7-1-2016

CHARACTERIZATION OF CARRIER TRANSPORT PROPERTIES IN STRAINED CRYSTALLINE SI WALL-LIKE STRUCTURES AS A FUNCTION OF SCALING INTO THE QUASI-QUANTUM REGIME

Clay Mayberry

Clay Scott Mayberry

Candidate

Nanoscience and Microsystems

Department

This dissertation is approved, and it is acceptable in quality and form for publication:

Approved by the Dissertation Committee:

, Chairperson

CHARACTERIZATION OF CARRIER TRANSPORT PROPERTIES IN STRAINED CRYSTALLINE SI WALL-LIKE STRUCTURES AS A FUNCTION OF SCALING INTO THE QUASI-QUANTUM REGIME

by

CLAY SCOTT MAYBERRY

B.S.E.E., University of New Mexico, 1990
M.S.E.E., University of New Mexico, 1993

DISSERTATION

Submitted in Partial Fulfillment of the
Requirements for the Degree of

Doctor of Philosophy
Nanosciene and Microsystems Engineering

The University of New Mexico
Albuquerque, New Mexico

July, 2016

DEDICATION

I dedicated this work to my family, my wife Lynn Ling-Yi, and my daughter Lee, who patiently endured my time away from them while pursuing this degree.

Acknowledgments

I whole-heartedly acknowledge Professor Ashwani Sharma's inspiration and motivation to pursue this degree. His drive and commitment to the fields of engineering and education, his desire to improve the state of the art of technologies, and loyalty to his friends and co-workers are to be admired.

I would like to especially thank Professor Danhong Huang who accomplished the theoretical work, his skill with solid state physics is astounding and he is an absolute pleasure to work with.

I also thank Professor Ganesh "Gunny" Balakrishnan, for his constant encouragement, fine practicality, sense of humor, and his wisdom that is significantly more advanced than his years.

I would like to give a special thanks to Professor Paul Sharma for his encouragement and enthusiastic support of this endeavor.

Finally, I would like to thank the dissertation committee members, Professor Christos Christos Christodoulou, Professor Ganesh Balakrishnan, Professor Ashwani Sharma, Professor Adam Hecht, and Professor Dan Huang.

Characterization of carrier transport properties in strained crystalline Si wall-like structures as a function of scaling into the quasi-quantum regime

By

Clay Scott Mayberry

B.S.E.E., University of New Mexico 1990

M.S.E.E., University of New Mexico, 1993

Ph.D., Nanoscience and Microsystems Engineering,

University of New Mexico, 2016

Abstract

The transport characteristics of both electrons and holes through narrow constricted “wall-like” Silicon (Si) long-channels that were surrounded by a thermally grown SiO_2 layer was investigated. As a result of the existence of fixed oxide charges in the thermally grown SiO_2 layer and the Si/SiO_2 interface, the effective Si cross-sectional wall widths were considerably narrower than the actual physical widths, due the formation of depletion regions from all sides. The physical height of the crystalline-Si structures was ~1500nm, and the widths were incrementally scaled down from ~200nm to ~20nm. These nanostructures were

configured into a metal-semiconductor-metal (MSM) device configuration that was isolated from the substrate. Dark currents, dc-photo-response, and time response measurements using a mode-locked femtosecond laser, were used in the study. In the narrowest wall devices, a considerable increase in conductivity was observed as a result of higher carrier mobilities due to lateral constriction. The strain effects, which include the reversal splitting of light- and heavy- hole bands as well as the decrease of conduction-band effective mass by reduced Si bandgap energy, are formulated in our microscopic model for explaining the experimentally observed enhancements in both conduction- and valence-band mobilities with reduced Si wall thickness. Specifically, the enhancements of the valence-band and conduction-band mobilities are found to be associated with different aspects of physical mechanisms. The role of the biaxial strain buffering depth is elucidated and its importance to the scaling relations of wall-thickness is reproduced theoretically, i.e., $1/L^2$ for electrons and $1/L$ for holes.

Contents

List of Figures

List of Tables

Chapter 1

INTRODUCTION

1.1 Motivation

For over 40 years, the microelectronics market place has driven the very large scale integration (VLSI) industry to make continuous improvements in computational power, bandwidth, and speed (1). These continued enhancements in performance have come in the form of “cramming” more components onto integrated circuits, as was predicted in 1965 by Moore (2). The push to increase the speed and density of the transistors on a chip has come in the form of shrinking the transistor size, in particular, the channel length (3; 4) as governed by the following equations for planar field effect transistors:

$$I_{Dsat} = \frac{W}{2L}\mu_{eff}C_{ox}(V_{GS} - V_T)^2 \quad (1)$$

$$g_{msat} = \frac{\partial I_{Dsat}}{\partial V_{GS}} = \frac{W}{L}\mu_{eff}C_{ox}(V_{GS} - V_T) \quad (2)$$

$$f_T = \mu_{eff}\frac{V_{GS}-V_T}{L^2} \quad (3)$$

where I_{Dsat} is the saturation current or drive current for a planar FET, W g_{msat} is the transconductance, a small signal parameter, f_T is the unity gain bandwidth, W is the width of the device, L is the channel length, μ_{eff} is the carrier mobility

for either a p or n channel device, C_{ox} is the gate oxide capacitance, V_{GS} is the voltage applied to the gate, and V_T is the threshold voltage, a device parameter. Clearly, decreasing the channel length, L, is clearly in the industry's interest as it leads to increased performance and accommodates miniaturization and increased circuit density.

Reductions in channel length, however, have come with challenges, i.e., short channel effects (5). Short channel effects lead to higher leakage currents, poor signal-to-noise ratios, and instability during operation, such as loss of channel gate control. Had device parameters scaled according to Dennards' scaling laws, circuit power would have remained essentially flat (6). The short channel effects led to a continual increase in power according to equations 4, and 5:

$$P_{dyn} = C_{ox}V_{dd}^2 f \qquad (4)$$

$$P_{static} = I_{leak}V_{dd} \qquad (5)$$

where P_{dyn} is the dynamic power of the complementary metal oxide semiconductor (CMOS)circuit (Figure 1.1, an inverter and the fundamental unit of digital processors) or processor and is the result of charging and then discharging the gate capacitor with an energy $\frac{1}{2}C_{ox}V_{dd}^2$ at the operating frequency f.

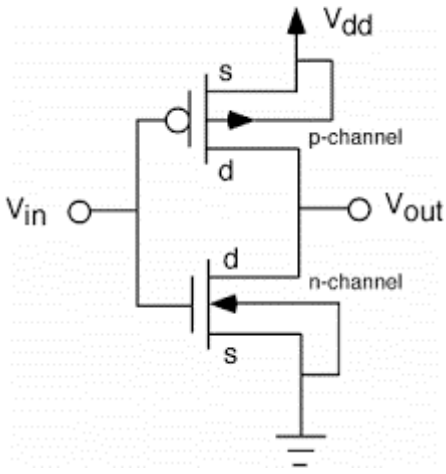

Figure 1.1 CMOS inverter circuit.

The static power, on the other hand, results from leakage current flowing from the voltage source V_{dd} to ground via paths through the channel and are termed subthreshold currents, paths around the channel through the body of the planar transistors, and Fowler-Norheim tunneling currents through the ever decreasing thickness of the gate oxide (7). Figure 2.2 depicts the evolution of these powers over time, and shows clearly how useful power did not stay flat but has grown and parasitic power has grown to become a significant part of the total circuit or processor power.

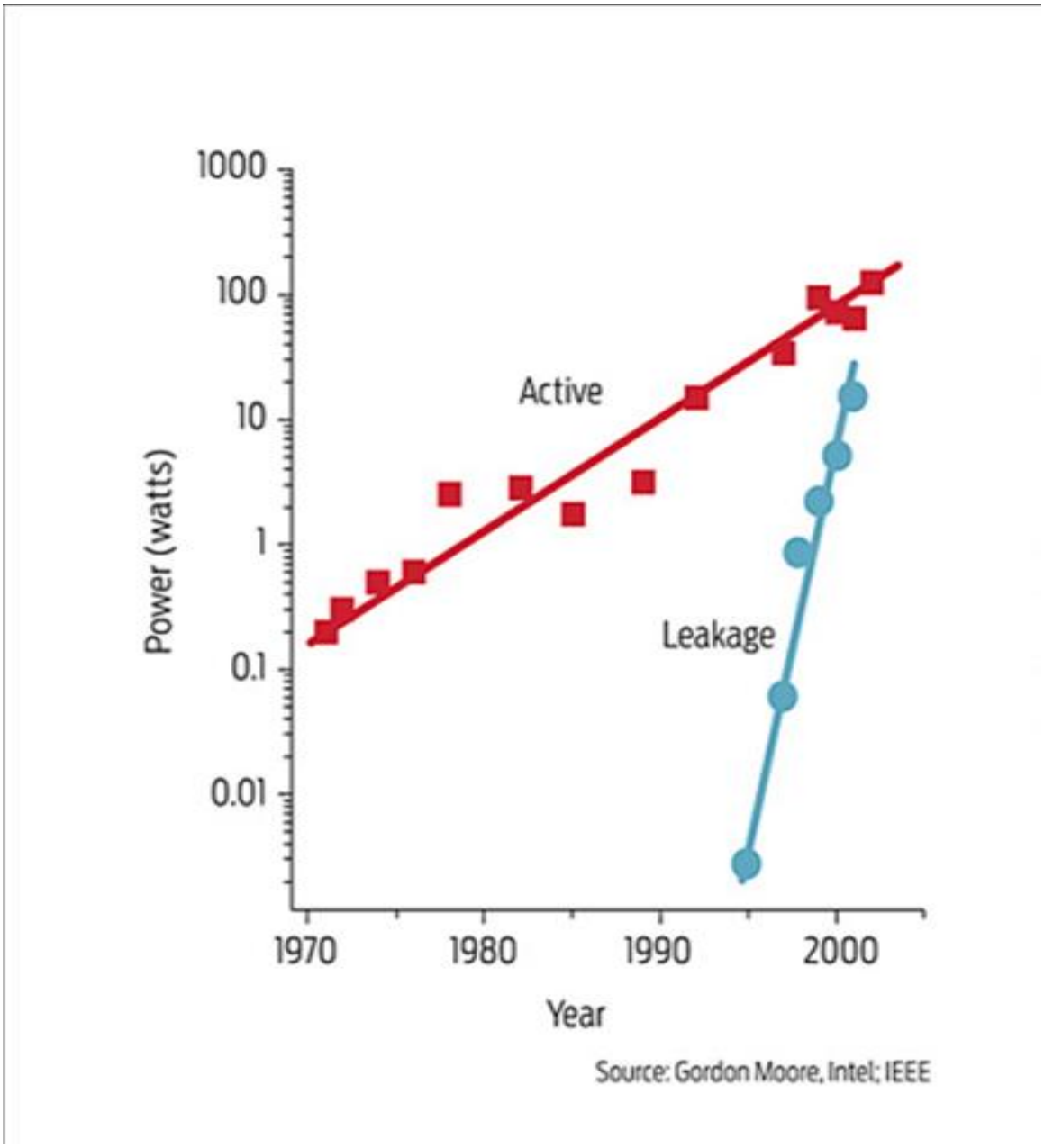

Figure 1.2 Evolution of useful and parasitic processor power over time.

In order to improve the transistor's gate control and switching speed, the contemporary CMOS industry has looked for alternative solutions to the

traditional planar transistor designs and substrates (8). Over the past several years, the CMOS industry has narrowed their focus into multi-gate field effect transistor designs (9) for improving the gate control, and strained substrates (10; 11) to enhance carrier mobilities and ultimately the switching speed and drive currents. One particular multigate transistor design, the FinFET (Figure 1.3), has gained considerable interest among the industry as a replacement (9). The FinFET has a tri-gate architecture and reductions of short-channel effects have been observed in these devices (12; 13).

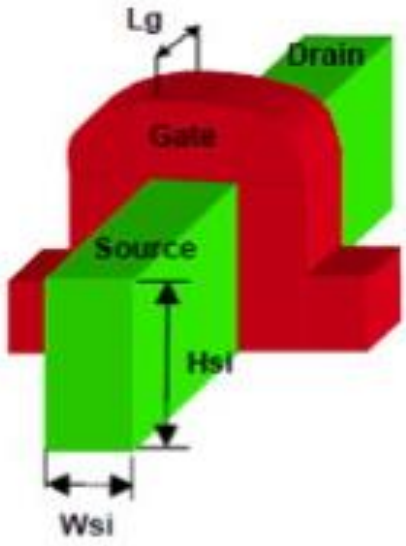

Figure 1.3 Schematic and layour of FinFET *(14)*.

This design provides gate control not only from the top of the channel, but also from the channel sides as well. This in itself improves the overall (on/off) gate control process; however, the drawback is that these devices require higher

operating voltages to achieve faster switching speeds (15). Bedell et al. (16) have reported that in the present FinFET technologies, the carrier mobilities are not seen to have been enhanced since the active region of these devices would require two opposite kinds of strain (i.e., tensile and compressive) on the same substrate, which would be possible by converting the tensile strain of silicon-on-insulator substrates to compressive strain in localized regions via a combination of selective SiGe (>40%) growth. Such FinFET devices have not yet been experimentally demonstrated. However, similar embedded silicon/germanium layered structures that would provide process induced stressors in the source and drain regions have been theoretically modeled. The results of these simulations show only a modest performance increase, approximately one-half enhancement in mobility, as compared to similar size planar FETs (17). Process induced strain in a FinFET would be most effective if it was directly under the gate region, as its stressor's effectiveness diminishes with depth. Incorporation of wafer level strain using SiGe-on-insulator (SGOI) and Strained Silicon-On-Insulator (sSOI) in small pitched circuits may be possible by converting the tensile strain of sSOI to compressive strain by selective growth of silicon-germanium. However, these types of configurations would certainly add complexities in a high volume manufacturing environment, which could negatively affect yield. In this dissertation, I report a comprehensive experimental and theoretical study on the nature of carrier transport, of both electrons and holes, through narrow constricted crystalline Si "wall-like" long-channels that were surrounded by a thermally grown SiO2 layer. The carrier

transport characteristics are evaluated as a function of dimensional scaling of the Si wall widths from 200 nm to 20 nm. The Si wall-widths were reduced by the process of thermal oxidation, where stress naturally accumulates in the channel. Basically, this structure configuration allows us to investigate the effects of strained regions that are “closing-in” from both sides. Additionally, as the wall-widths approach the quasi-quantum regime, the carriers start to become confined and therefore react to the narrow paths, and possibly behave more like waves than particles (18), thus altering the macroscopic nature of resistance, capacitance, and inductance to a more exotic microscopic one (19). However, this transition into the quantum mechanical regime does not come about abruptly. Rather, there is a transition region in which the bulk properties begin to slowly weaken while the quantum effects begin to strengthen. The effects of quantum confinement on carrier transport properties, however, have been primarily investigated in ternary and quaternary material heterostructures and superlattices, in which scattering is seen to enhance some modes of the electron-lattice interactions while suppressing others, thereby changing the relative value of the carrier’s effective masses of electrons and holes, as compared to bulk semiconductors (20). To date such studies in Si have been very limited. I believe that these wall structures are a useful starting point for a broader study, as these can be configured into novel high density 3-D VLSI devices, where thermal effects, such as heat buildup, can also be efficiently managed (21).

The dissertation is organized as follows: In Ch. 2, the process for fabricating the crystalline Si wall structures is described, and the two electrode, metal-semiconductor-metal device structure fabrication is also discussed. In Ch. 3 the experimental dc measurements as a function of wall width thickness are presented, including dark currents and photocurrents. The electron and hole transient time responses and analysis are explained in Ch 4. Chapter 5 provides a detailed model to explain the role of strain effects and how they impact both the electron and hole mobilities, while a summary is given in Ch. 6.

1.2 Description of Present Work

In this dissertation, the results of a study where the carrier transport properties are evaluated as a function of dimensionally scaling crystalline silicon active channel wall widths from ~200nm to ~20nm. The scaling was accomplished by the careful application of oxidation techniques on initially large structures using thermally grown oxidation which consumes the Si, thus reducing the width of the wall structures. The fabrication methods employed in the development of these test structures are completely within the methodologies and techniques of typical production semiconductor foundries and result in much simpler geometries and less complex devices. These wall structures take advantage of the lattice mismatch between the oxidation and the channel, the silicon dioxide serving as the stressing element naturally developing strain in the channel. These wall structures will serve as a starting point for a broader study, as these can be configured into novel high density 3-D devices with wrap-around gates achieving cylindrical geometry with a high

degree of sub-threshold current control. Controlling sub-threshold currents minimizes quiescent thermal effects, and the devices may lead to efficient switching minimizing dynamic heating (22). Additionally, the cylindrical geometry with a cylindrical gate oxide may diminish or eliminate the effects of oxide charging on the operation of a nanowire field effect transistor since the operation may rely on the electric fields between the gate and the source rather than channel inversion, a subject for follow-on investigations.

The analysis of the data obtained for carrier transport employs the results of a theoretical development by a colleague where not only the use of deformation potentials was employed, but conduction band bending, valence band splitting with split carrier populations, with competing forces on carrier mobilities resulting in substantial overall gains in carrier mobilities in very thin structures.

1.3 References

1. *Understanding Moore's Law: Four Decades of Innovation.* **Brock, D. C.** s.l. : Chemical Heritage Foundation, 2006.

2. *Cramming more components onto integrated circuits.* **Moore, Gordon.** 8, s.l. : Electronics, 1965, Vol. 38.

3. **Bohr, M.** s.l. : IEEE Solid-State Circuits Conference, Digest of Technical Papers, p. 23., 2009.

4. **Kuhn, K. J.** s.l. : Microelectron. Eng., 2011, Vols. 88, 1044.

5. **Fossum, S. Veeraraghavan and J. G.** s.l. : IEEE Trans. Electron Devices, 1989, Vols. 36, 522.

6. *Design of Ion-Implanted MOSFETs with Very Small Physical Dimensions.* **Robert Dennard, Fritz Gaensslen, Hwa-Nien Yu, Leo Ridout, Ernest Bassous, Andre LeBlanc.** 5, s.l. : IEEE Journal of Solid State Physics, 1974, Vols. sc-9.

7. **Balestra, F.** *Nanoscale CMOS: Innovative Materials, Modeling and Characterization.* London, England : John Wiley & Sons, 2010. ISBN: 978-1-84821-180-3.

8. **D. Hisamoto, T. Kaga, and E. Takeda.** s.l. : IEEE Trans. Electron Devices , 1991, Vols. 38, 1419.

9. **Mohanram, M. Rostami and K.** s.l. : IEEE Trans. Comput. Aided Des. Integr. Circuits Syst., 2011, Vols. 30, 337.

10. **H. M. Manasevit, I. s. Gergis, and A. B. Jones.** s.l. : J. Electron. Mater. , 1983, Vols. 12, 637.

11. **N. Xu, B. Ho, M. Choi, v. Moroz, and H. J. King Liu.** s.l. : IEEE Trans. Electron Devices, 2012, Vols. 59, 1592.

12. **M. Veshala, R. Jatooth, and K. R. Reddy.** s.l. : Int. J. Eng. Innovative Technol. , 2013, Vols. 2, 118.

13. **X. Huang, W. C. Lee, C. Kuo, D. Hisamoto, L. Chan g, J. Kedzierski, E. Anderson, H. Takeuchi, Y. K. Choi, and K. Asano.** s.l. : IEEE Trans. Electron Devices , 2001, Vols. 48, 880.

14. s.l. : http://electronics.stackexchange.com/questions/37212/short-channel-effects-and-finfet.

15. **L. Chang, D. J. Frank, R. K. Montoye, S. J. Koester, B. L. Ji, P. W. Coteus, R. H. Dennard, and W. Haensh.** s.l. : Proc. IEEE, 2010, Vols. 98, 215.

16. **S. W. Bedell, A. Khakifirooz, and D. K. Sadana.** s.l. : MRS Bull., 2014, Vols. 39, 131.

17. **Y. Sun, S. E. Thompson, and T. Nishida.** s.l. : J. Appl. Phys., 2007, Vols. 101, 104503.

18. **Ferry, D. K.** 61, s.l. : Superlattices Microstruct., 2000, Vol. 27.

19. **Ahmed, N. J. Stone and H.** 2134, s.l. : Appl. Phys. Lett, 1998, Vol. 73.

20. **Ghatak, S. Bhattacharya and K. P.** *Effective Electron Mass in Low-Dimensional Semiconductors.* New York : Springer, 2013.

21. **M. C. Cheng, J. A. Smithy, W. Jia, and R. Coleman.** 202, s.l. : IEEE Trans. Electron Devices , 2014, Vol. 61.

22. *Effects of dimensional scaling on the electronic transport properties of silicon nanofilms and nanowires.* **A. K. Sharma, R. Prinja, S. R. J. Brueck.** s.l. : 5th IEEE Conference on Nanotechnology, 2005, Vol. 2.

Chapter 2 FABRICATION

2.1 Rationale for Substrate Material

Silicon on insulator (SOI) wafers with a top active layer of ⟨100⟩ (Figure 2.1) crystal orientation were used to fabricate the wall-like structured devices for this study. The initial SOI wafer was procured with a 1500 nm active layer on top of a 3000 nm buried oxide (Figure 2.2). A scanning electron microscope (SEM) image of an actual wafer before processing is shown in Figure 2.3. The SOI configuration with the insulating dielectric layer allowed complete electrical isolation of the Si wall-like structures from the underlying substrate, in other words, the devices are configured within the 1500 nm top active layer. Several types of processing techniques were applied to this structure including oxidation and etching to down-scale the wall widths of the final devices. The rate of oxidation is a function of the particular crystallographic direction in which it is

applied (1), and an experimenter must be aware of the surrounding structure; the orientation for this wafer is shown in Figure 2.4.

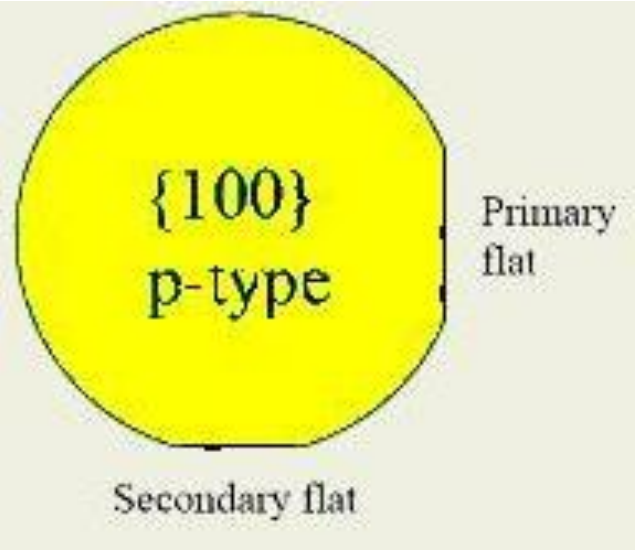

Figure 2.1 Silicon on insulator wafer with {100} indications (flats).

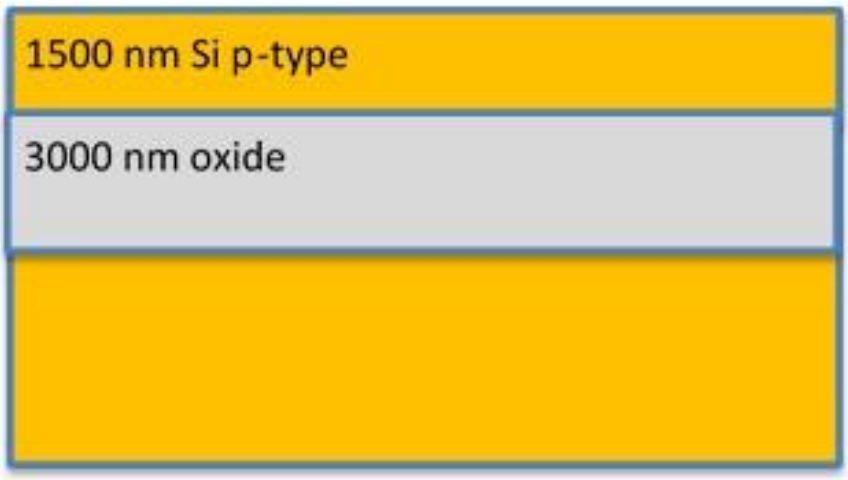

Figure 2.2 Silicon on insulator wafer cross-sectional layout and thicknesses of oxide and active layer.

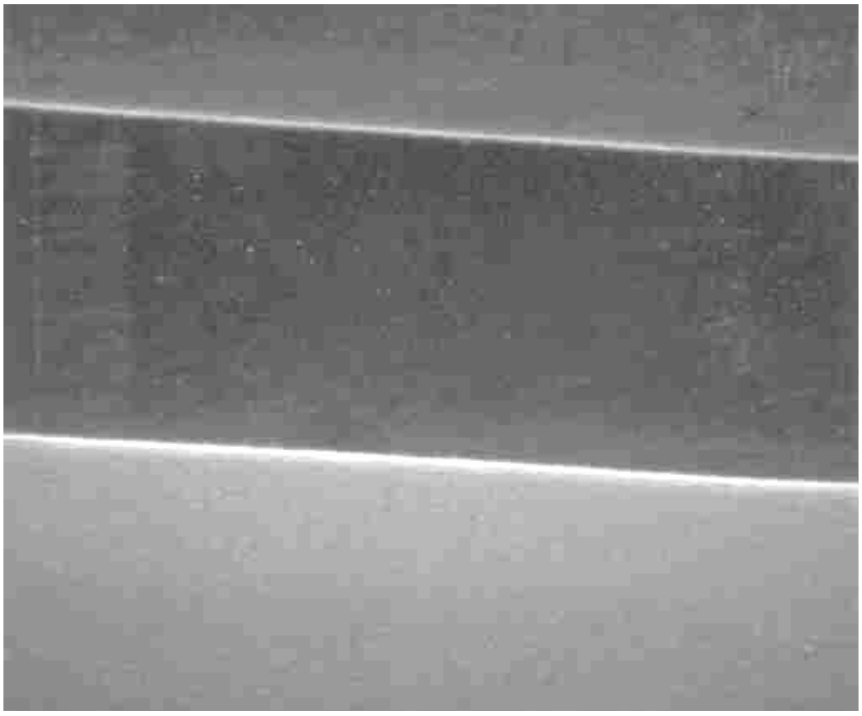

Figure 2.3 SEM photograph of SiO2 wafer before processing.

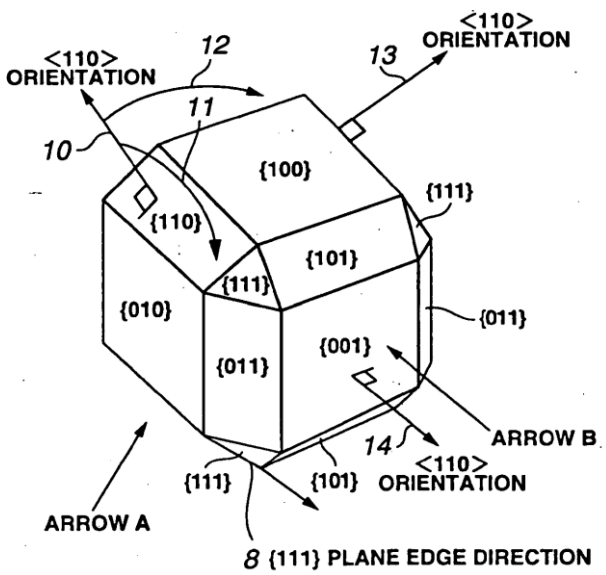

Figure 2.4 Crystallographic orientation of the SiO_2 wafer used for this study (2).

All five samples in this study had an identical p-type active layer with a lightly doped concentration of $10^{14}/cm^3$ boron atoms. Intrinsic SOI wafers would have been an ideal choice for the experiment, however, due to the commercial unavailability of 100% intrinsic material, the above choice of dopant type and concentration was adequate enough to minimize the effects of impurity scattering. Boron tends to segregate away from the Si interface and into the thermally grown oxide (3), thus reducing the impurity concentration near the Si interface with SiO_2. Thus the segregation coefficient, which is defined as the ratio of the dopant concentrations in the oxide and silicon at the interface, is less than one in this case. The thermal oxidation process leads to the formation of an oxide trapped charge (Q_{ot}), which contributes to the formation of a depletion region

near the Si/SiO_2 interface (4; 5). When this oxide trapped charge is combined with the fixed charge (Q_f) which naturally results from the excess Si atoms not reacted with the oxygen, and the interface trapped charge (Q_{it}) which results from the mismatch between the number of atomic bonds in the Si crystal surface and the number of available bonds in the SiO_2 layer, the total charge associated with the interface and oxide layer is $Q_{ot} + Q_f + Q_{it}$. This charge forms a depletion region in Si that extends several nanometers away from the SiO_2 interface (5; 6). Thus the effective Si cross-sectional wall widths were considerably narrower than the actual physical widths, due this formation of depletion regions from both sides.

2.2 Crystalline Silicon Wall Nanostructure Fabrication

In order to fabricate the wall structures, photoresist nano-scale pattering was required. The precursors to the wall structures were patterned using interferometric lithography (IL) (7) and reactive-ion-etching (RIE) (8; 9). IL is a well-developed technique for inexpensive photoresist nano-patterning (10). A typical IL laboratory setup, shown in Figure 2.5, consists of a collimated laser beam incident on a Fresnel mirror (FM) arrangement (11), passed through a spatial filter, and mounted on a rotation stage for period variation. IL, in its simplest form, is interference between two coherent waves resulting in a 1D periodic pattern defined by

$$\lambda/2sin\theta \qquad (1)$$

where λ is the optical wavelength and 2θ is the angle between the interfering beams, as shown in Figure 2.6. As shown in Figure 2.6, there is no $\hat{z}$-dependence to an IL exposure pattern, which is limited only by the laser coherence length and beam overlaps (12), and therefore produces a columnar pattern in the photoresist as shown in Figure 2.7.

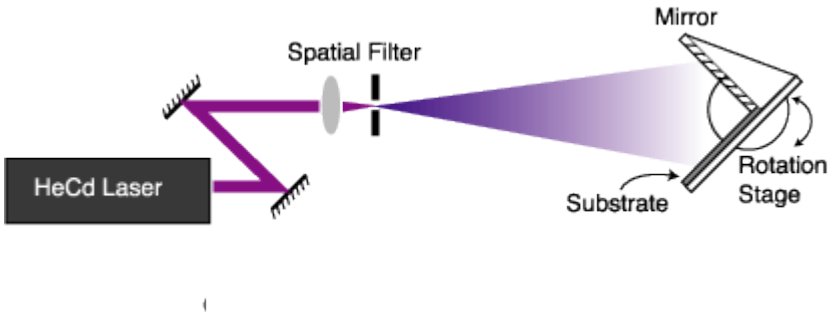

Figure 2.5 Typical interferometric lithography system used to produce initial patterns (13).

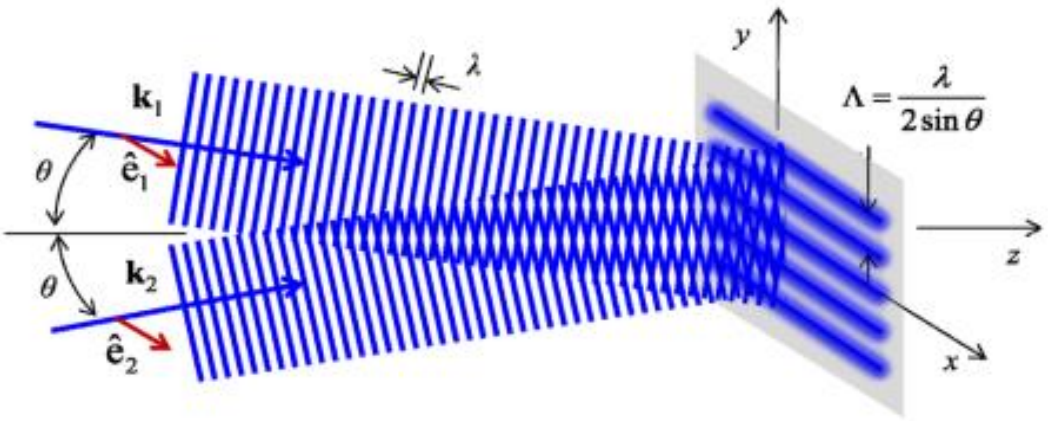

Figure 2.6 Two-beam interference. Interference fringes at the x-y plane with a periodicity of Λ are formed by two linearly-polarized, monochromatic, plane waves.

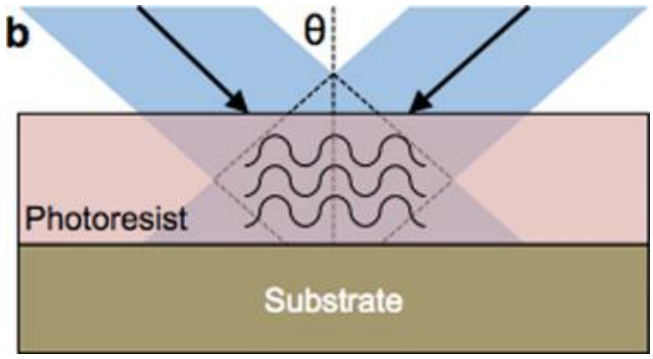

Figure 2.7 Interference lithography exposure pattern in photo-resist.

The 1D nanoscale patterns were first formed in the photoresist (Figure 2.8) and followed by pattern transfer onto the underlying substrate with reactive ion etching (RIE) in a parallel plate reactor using SF6 plasma chemistry. Figure 2.9 shows a schematic of a reactive ion etching system. In an RIE system, the chamber is grounded, radio-frequency at 13.6 MHz is applied to the chamber at sufficient power to ionize the SF_6 gas in the following reaction (14)

$$e + SF_{x_g} \rightarrow SF_{x-1_g} + F_g + e. \qquad (1)$$

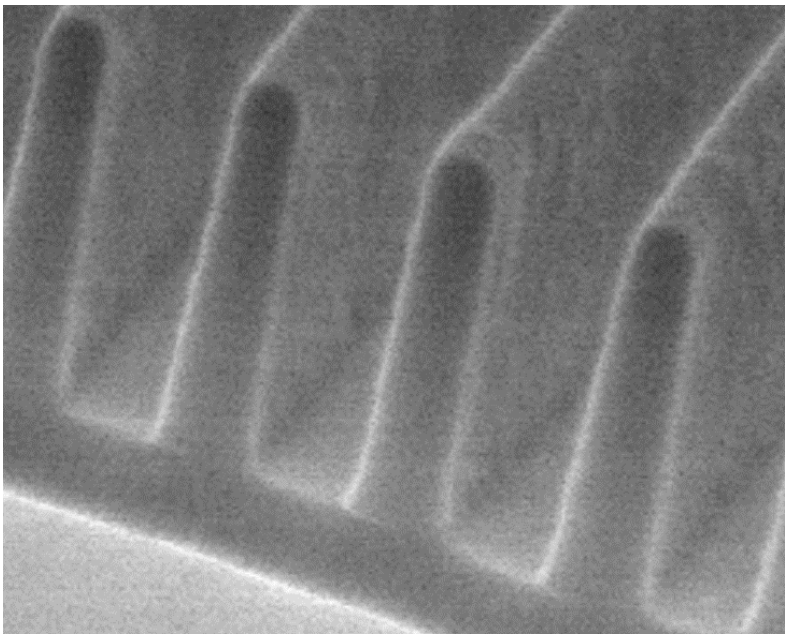

Figure 2.8 SEM photograph of 1D nanoscale patterns formed in the photoresist.

The electrons, being light and agile, move to the silicon target and charge the silicon producing an electric field between the silicon and the plasma. The resulting electric field causes the more massive ions to move to the substrate and isotropic chemical etching occurs with the following reaction

$$Si + 4F \rightarrow SiF_4. \qquad (2)$$

RIE has the capacity to produce anisotropic physical etching under the correct gas pressures where the ions bombard the surface and remove atoms. Therefore, following the correct procedures anisotropic etching was used to transfer the photolithographic pattern to the underlying silicon.

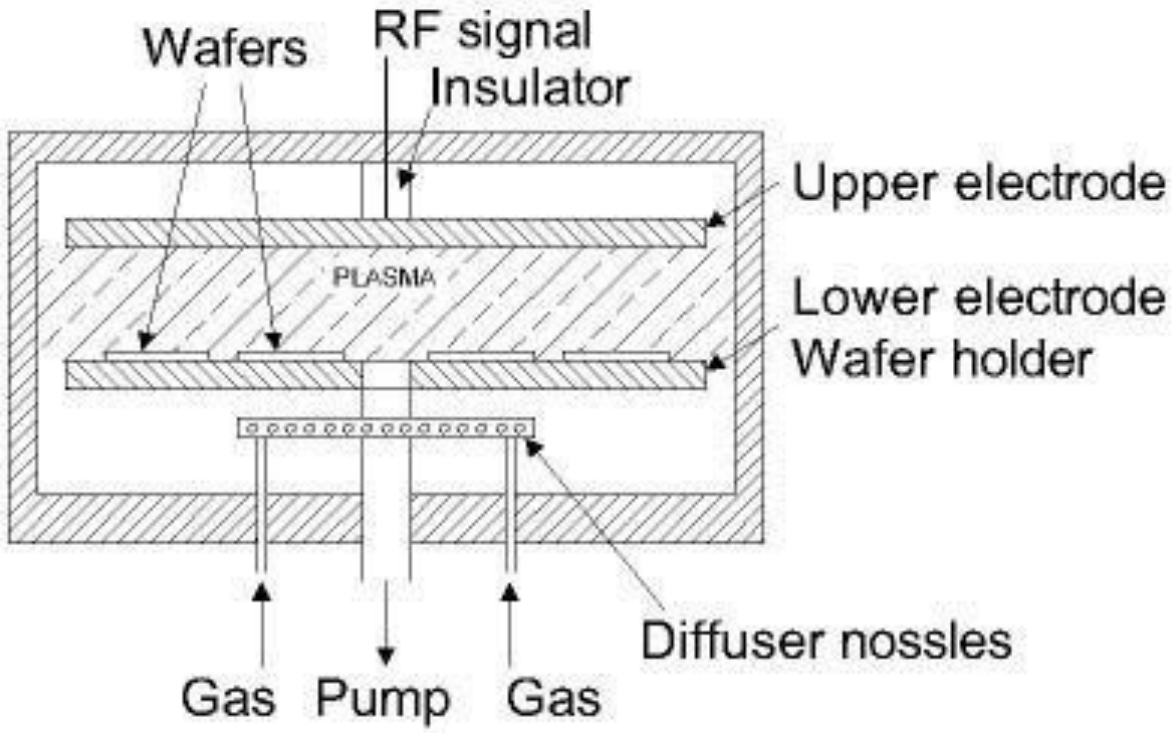

Figure 2.9 Operation and layout of reactive ion etching chamber (15).

Figure 2.10 shows a SEM cross-sectional image of an array of nano-wall structures with a remaining layer of patterned photoresist after RIE has been performed. Note at this stage these structures are merely the precursors to the thin Si wall structures that are then reconfigured into a

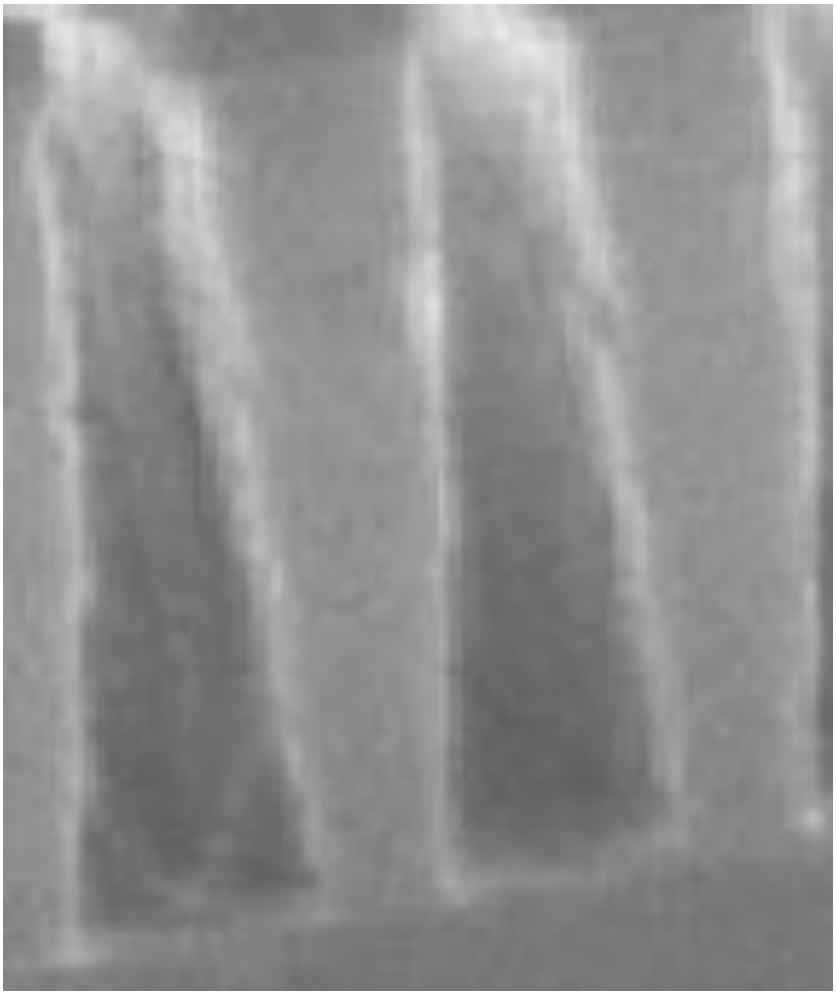

Figure 2.10 Initial wall structures that result from IL and RIE.

metal-semiconductor-metal (MSM) devices. After the photoresist was removed, the wall structures are thermally oxidized. The oxidation process accomplished two things. First, it consumes the Si, and thus thins the wall width. Second, the thermally grown oxide preserves a low defect, clean Si/ SiO_2 interface, and at the same time passivates the surfaces of the nanostructures (12; 16). The Si/SiO_2 interface has low defects, and it is important to note that strain is present at the interface and it reduces with distance from the interface. This reduction in strain as a function of depth has been seen experimentally in Si/SiO_2 interfaces using a scanning transmission electron microscope using Z-contrast imaging which produces strain contrast imaging (17). Using this technique, the $1/e$ decay length was measured at approximately 1 nm. As noted above, the modeling of the thermal oxidation parameters needed for the desired active channel thickness was complicated due to the fact that in a three dimensional wall structure there are several crystal lattice orientations that have different thermal oxidation rates. As a first order approximation, the average values of oxidation rates between the various lattice orientations, i.e., oxygen flow rate, pressure, temperature, and time were used. These parameters were then fine-tuned empirically during the actual thermal oxidation runs. Figures 2.11–2.13 show SEM images of the cross-sectional views of the wall structures after the respective thermal oxidations. As can be seen from the SEM images, due to the high aspect ratio of these structures the oxidation rate was not fully uniform throughout the height of the walls. The rate was faster at the top part of the walls and slower at the bottom part due to higher availability of oxygen atoms in the upper regions. The resulting

wall-like Si structures surrounded by the thermally grown oxide are then configured into the active region of the MSM devices as described in the next section.

Figure 2.11 SEM cross sectional view of 200 nm channel wall structure.

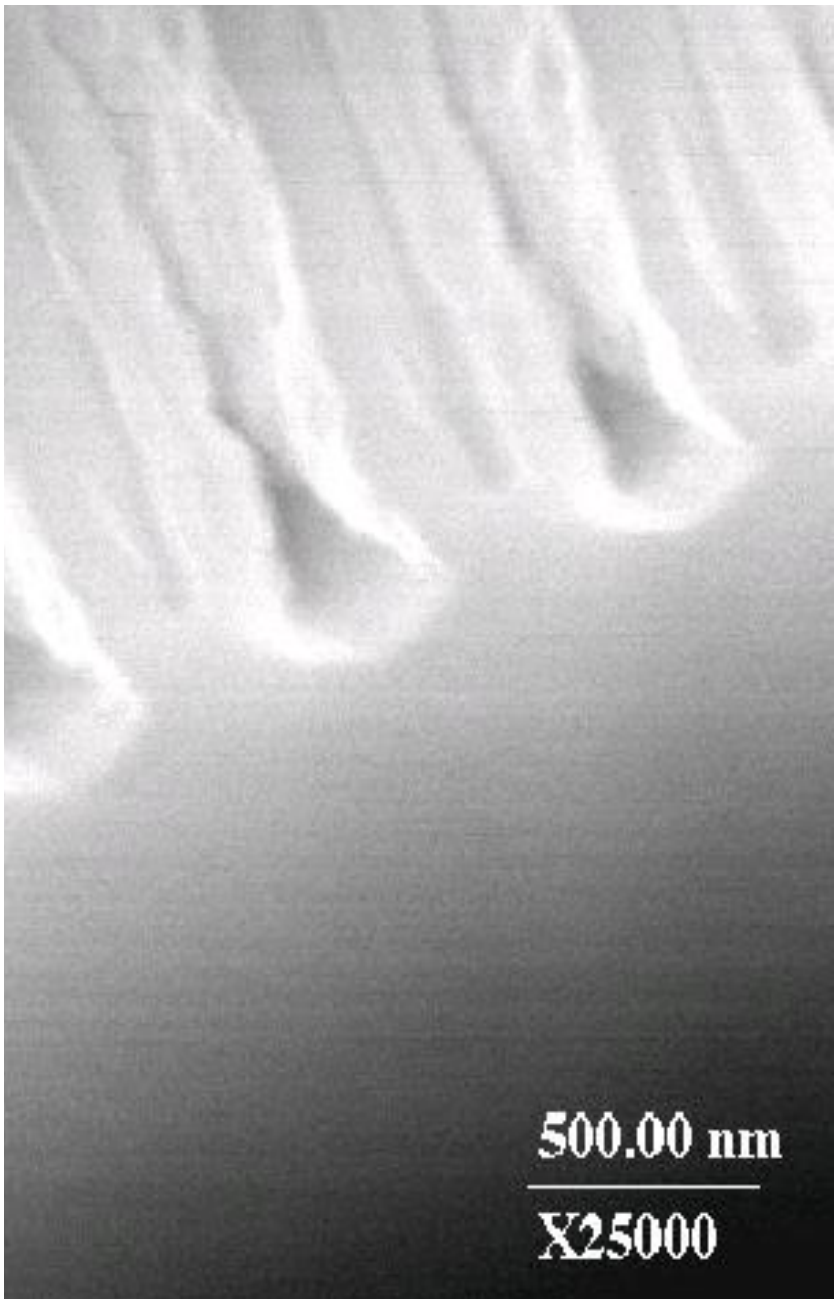

Figure 2.12 SEM cross sectional view of 95 nm channel wall structure.

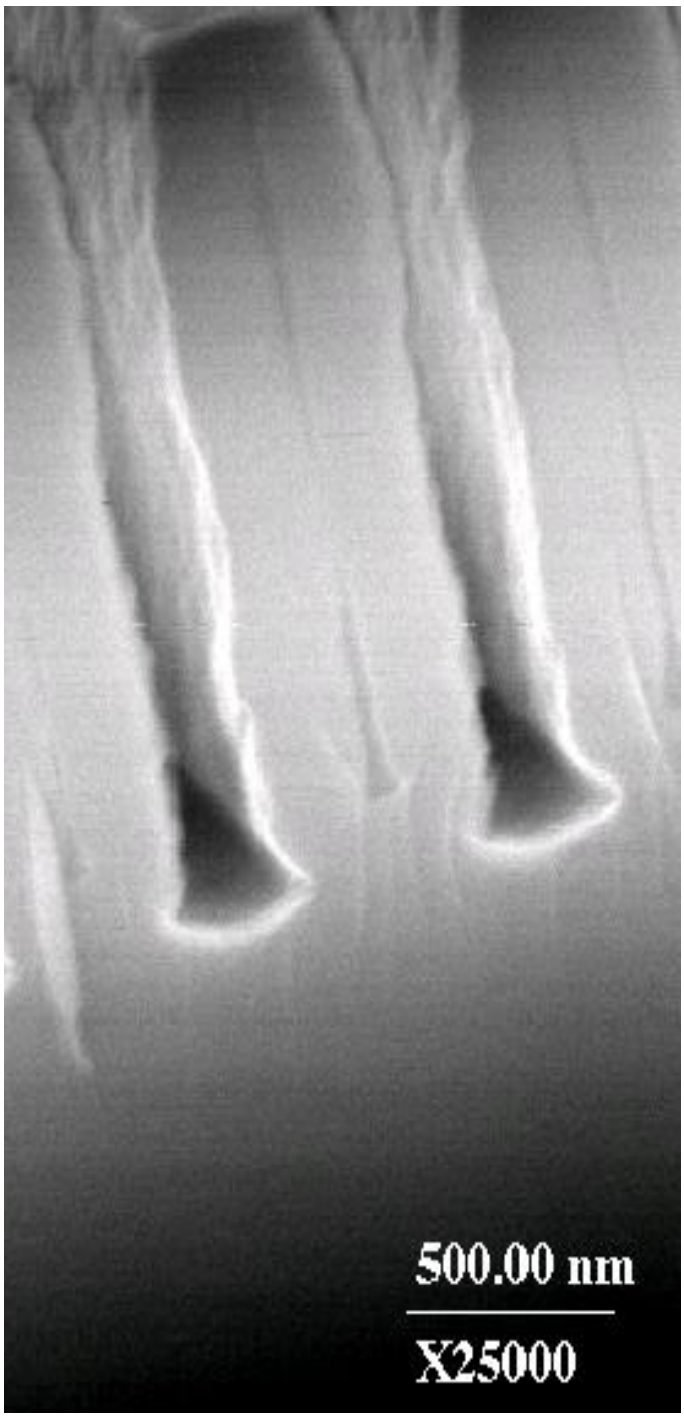

Figure 2.13 SEM cross sectional view of 40 nm channel wall structure.

2.3 MSM Device Fabrication

The wall structured samples were configured into two terminal metal-Si/nanowall-metal (i.e., MSM) devices for optical and electrical characterization. The MSM device configuration was specifically designed so the total current would flow within the wall boundaries between the electrodes. This allowed the physical cross-section of the wall structures to dictate the current flow properties. The mesa structures were fabricated to cut off any stray current paths that could bypass the intended active region (wall) carrier path. After the walls were oxidized to achieve the desired wall width, the thermally grown oxide was selectively removed from the planar un-textured Si pad locations (Figure 2.14) using an appropriate photo-mask and a chemical 1:6 buffered oxide etch (BOE) process. Following the resist removal, the samples were cleaned using a sulfuric-acid/hydrogen-peroxide solution, and a DI (deionized) water rinse followed by a nitrogen gas dry step. The samples were then re-patterned using photoresist, and a second mask was used in the process to form the electrode contact regions. Three separate evaporations (30 nm of Ni) were performed. The first one was performed at a normal incidence to the sample surface and the other two at a $30°$ tilt angle in order to ensure complete coverage of the mesa step height. After Ni evaporation, liftoff was performed to remove the unwanted metal and resist using acetone. Following a thorough rinse using methanol/DI-water, the samples were again dehydrated and spin-coated with a thick resist layer. The samples were patterned using a final metallization mask set. A layer of Cr and Au was evaporated on the electrode regions. 30 nm/200 nm of Cr/Au were

evaporated and liftoff process was used to remove the resist and unwanted metal. Figure 2.15 is a SEM photograph of silicon mesas surrounded by oxide with metallized contacts. Figure 2.16 shows SEM pictures of a fully fabricated wall device suitable for electrical characterization.

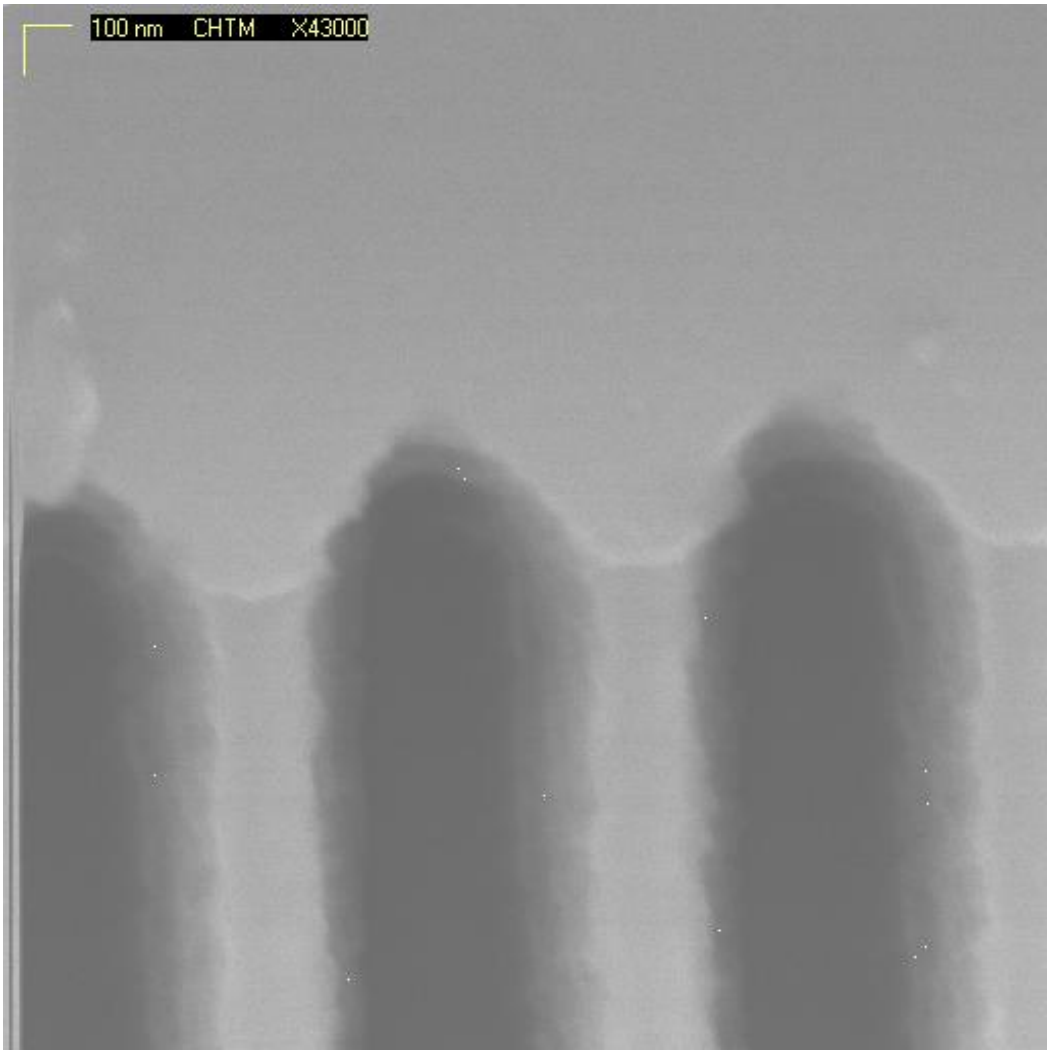

Figure 2.14 Oxide removal from electrical pad area, ready for subsequent electrical contact formation.

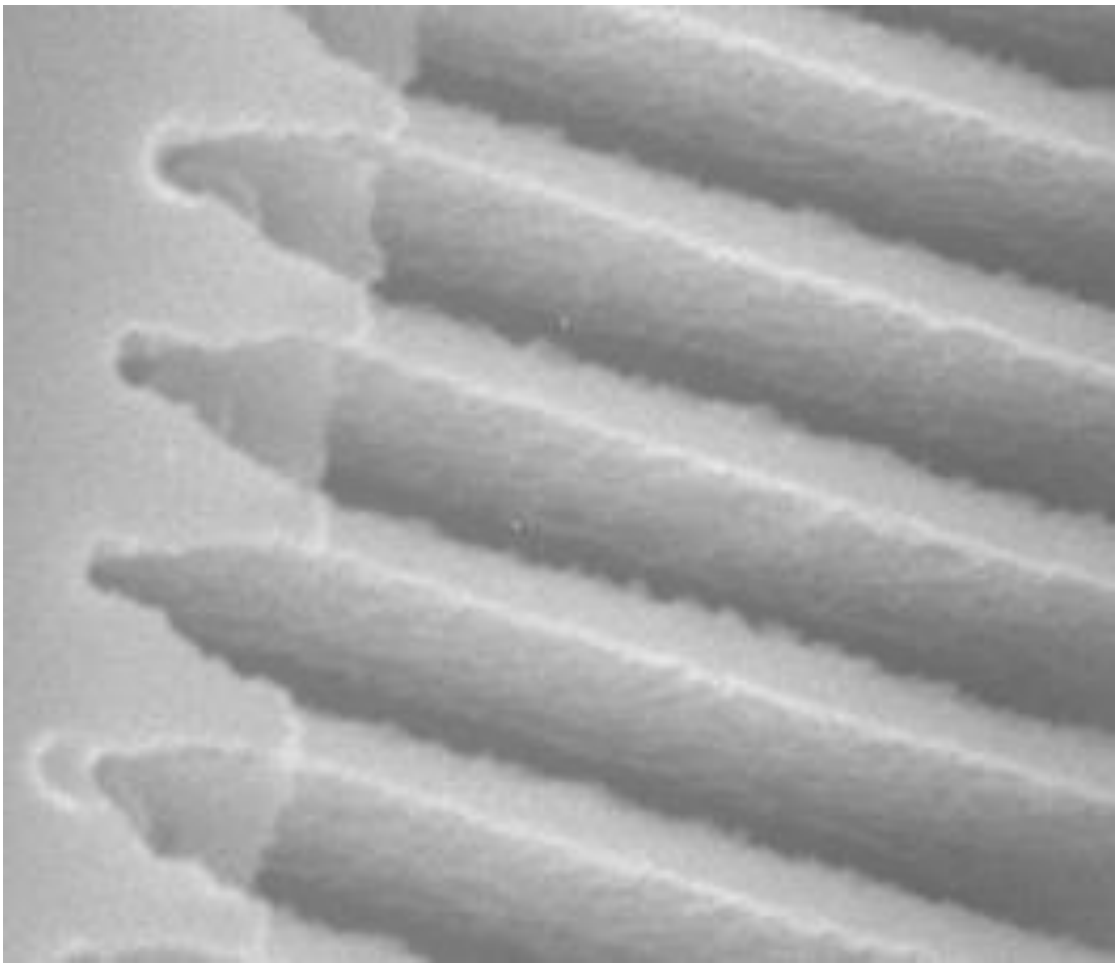

Figure 2.15 SEM photograph of silicon mesas surrounded by oxide with metallized contacts.

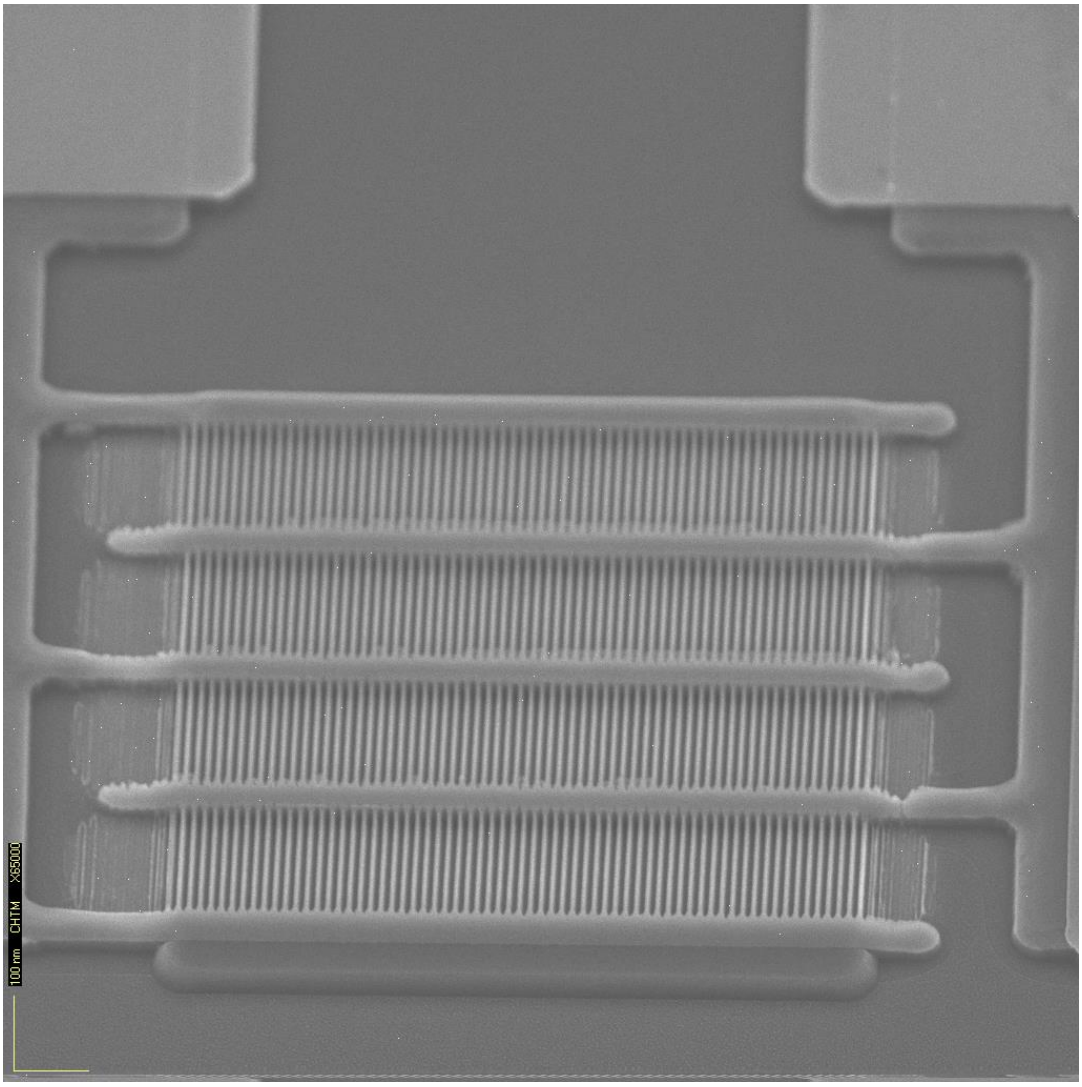

Figure 2.16 SEM photograph of completed MSM devices.

2.4 References

1. **Campbell, Stephen A.** *Fabrication Engineering at the Micro- and Nanoscale 4th Edition.* Oxford, NY : Oxford University Press, 2013. ISBN: 978-0-19-986122-4.

2. **Tetsuhiro KOMATSU DENSHI KINZOKU K. K. Iida, Yutaka KOMATSU DENSHI KINZOKU K. K. Shiraishi, Ryota KOMATSU DENSHI KINZOKU K. K. Suewaka, Junsuke KOMATSU DENSHI KINZOKU K. K. Tomioka,.** *Single crystal silicon producing method, single crystal silicon wafer and ingot produced thereby.* Washington, DC : Patent Application: EP 1498516 B1, 2011.

3. **Tauber, S. Wolf and R. N.** *Silicon Processing, 2nd ed. Vol. 1.* Sunset Beach, CA : Lattice Press, 2000.

4. *First-Principles Study of Boron Diffusion in Silicon.* **W. Windl, M. M. Bunea, R. Stumpf, S. T. Dunham, M. P. Masquelier.** s.l. : Phys. rev. Lett. 83 4345, 1999.

5. *Carrier transport near the Si/SiO2 interface of a MOSFET.* **W. Hansch, T. Vogelsang, R. Kircher, M. Orlowski.** s.l. : Solid-State Electron, 1989, Vol. 32.

6. **Yang, E. S.** *Microelectronic Devices.* s.l. : McGraw-Hill, Inc., 1988. 0-07-072238-2.

7. *Interferometric lithography for nanoscale fabrication.* **S. H. Zaidi, S. R. J. Brueck.** s.l. : SPIE, 1999, Vol. 3618.

8. ***M. Zhang, J. Z. Li, I. Adesida, and E. D. Wolf.*** *s.l. : J. Vac. Sci. Technol. B 1, Vols. B-1.*

9. ***A. J. van Roosmalen, J. A. G. Baggerman, and S. J. H. Brader.*** *Dry Etching for VLSI. s.l. : Springer Science & Business Media LLC, 1991.*

10. ***Brueck, X. Chen and S. R. J.*** *s.l. : J. Vac. Sci. Technol. 3392, 1998, Vol. B 16.*

11. ***A. J. Bourdillon, C. B. Boothroyd, J. R. Kong, and Y. Vladimirsky.*** *s.l. : J. Phys. D: Appl. Phys. 2133 , 2000, Vol. 33.*

12. Interferometric lithography exposure tool for 180-nm structures. ***S. H. Zaidi, S. R. J. Brueck, F. M. Schellenberg, R. S. Mackay, K. Uekert, J. J. Persoff.*** *s.l. : SPIE Proceedings Novel Lithographic Technologies, 1997, Vol. 3048.*

13. ***s.l. : http://nanoweb.mit.edu/annual-report01/07.html.***

14. Anisotrapic Reactive Ion Etching of Silicon Using SF6/O2/CHF3 Gas Mixtures. Rob Legtenberg, Henri Jansen, Meint de Boer, and Miko Elwenspoek. 6, s.l. : J. Electrochem. Sac., 1995, Vol. 142.

15. http://greiner227.blogspot.com/. Website accessed 4May2016.

16. Defects in SiO2/Si Structures Formed by Dry Thermal Oxidation of RF Hydrogen Plasma Cleaned Si. S. Alexandrova, A. Szekeres, E. Halova. s.l. : Materials Science and Engineering (IOP Publishing) , 2010, Vol. 15.

17. G. Duscher, S. J. Pennycook, N. D. Browning, R. Rupangudi, T. Takoudis,H.-J. Gao, and R. Singh,. s.l. : AIP Conf. Proc. 449, 191, 1998.

Chapter 3

ELECTRICAL AND OPTICAL STEADY STATE MEASUREMENTS

3.1 Dark Current Measurements

At room temperature and at thermal equilibrium conditions only a small number of carriers are thermally generated (as dark current) for a Si bandgap of 1.15 eV. At low bias voltages (linear region of operation), the slope of the current versus voltage (I-V) dark current is proportional to the device resistance and material resistivity as shown in equation 1,

$$\rho = \frac{1}{\sigma} = \frac{1}{q(n\mu_n + p\mu_p)} \qquad (1)$$

where ρ is the resistivity in $\Omega - cm$, σ is the conductivity in Siemens/cm (S/cm), q is the electronic charge, n and p are the concentrations of electrons and holes respectively in cm^{-3}, μ_n and μ_p are the carrier mobilities in $cm^2/v - s$. The dark current includes contributions of thermally generated carriers from both the wall channels and the metal/semiconductor contact regions. The current density, resistance, and total current, follow the following linear relationships as shown in equations 2, 3 and 4

$$J = \sigma E \qquad (2)$$

$$R = \frac{\rho l}{wh} \qquad (3)$$

$$I = RV \qquad (4)$$

where J is the current density in amps/m^2, E is the electric field in volts/meter, l, w, h are the length, width, and height of a material with l in the direction of current flow and the electric field, R is the resistance in ohms, I is the total current in coulombs/sec, and V is the applied potential in volts.

At higher biases (higher applied voltage, V), the current saturates when all thermally generated carriers are collected. Any further increase in the current can be attributed to leakages across the contact metal-semiconductor barrier and to nonlinear generation of carriers across the barrier (1). The back interpolation of this leakage current to the zero bias (0 V) condition is a measure of the saturated dark current (I_{ds}).

The thermal equilibrium condition can be perturbed by the process of carrier injection by either optical or electrical means (2). When the semiconductor is illuminated with photons having energy greater than the bandgap energy, $E = h\nu > E_g$, in this case $E_g = 1.15\ eV$ for silicon, electrons can be elevated to the conduction band leaving a hole in the valence band, and both contribute to conduction as in equation 1.

A semiconductor's carrier population under illumination establishes a new equilibrium when the rate of generation of carriers equals the recombination of carriers. Although the photocurrents in the presence of a bias are a few orders of magnitude larger than the thermally generated dark currents, the analysis of the photocurrent (I_{ps}) I-V function is the same as the dark current (I_{ds}) IV plots. For dc

response analysis, two sets of measurements were performed. These include: (i) dark currents as a function of wall width thickness, and (ii) photocurrents as a function of wall width thickness. These results are discussed and analyzed below.

3.2 Dark Current Versus Wall Width Thickness

To study the carrier conduction properties versus dimensionally scaling down the width of the wall structures into the nano-regime, the samples were characterized in batches. Using samples with wall widths of 200 nm, 95 nm, 75 nm, 40 nm, and 20 nm, the room temperature dark currents were measured with a probe station and digital I-V curve tracer.

As shown in Figure 3.1, only the physical cross-sectional area of the wall widths was reduced, and that by reducing the width ‘w’ from 200 nm to 20 nm. From Ohm’s law, equation 4, the resistance is inversely proportional to the cross-sectional area, and in particular to ‘w,’ and should therefore increase as the area is reduced since all other parameters of equation 4 are constant including the resistivity (in units of $\Omega - cm$). However, as can be seen from the Figure 3.2, the resistivity is not constant but drops significantly as the width of the wall is reduced below 95 nm. This reduction in resistivity suggests that there is an increase in conductivity as the wall thickness decreases from 95 nm to 20 nm. The conductivity is a function of carrier mobility and density as shown in equation 5.

$$\sigma = q(\mu_n n + \mu_p p) \qquad (5)$$

where μ_n is the electron mobility and μ_p is the hole mobility, n is the electron carrier density in cm^{-3}, p is the hole density. The mobility is a function of carrier velocity and electric field as shown in equation 6

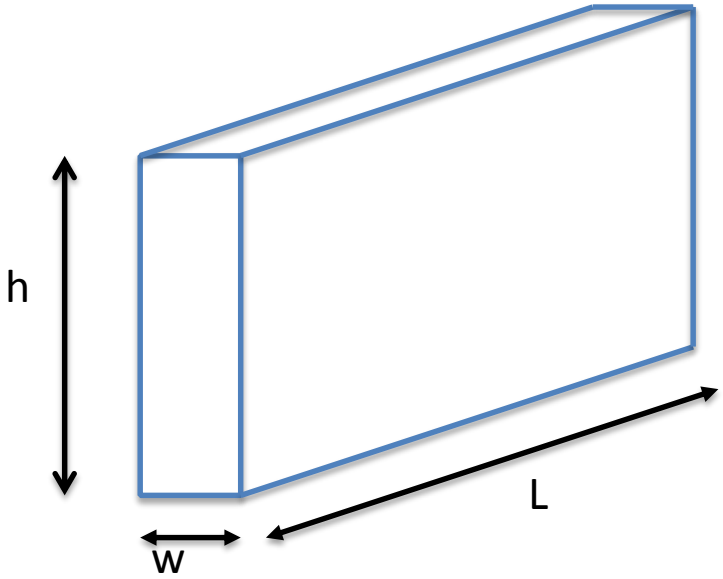

Figure 3.1 Geometry of crystalline silicon wall structure, dimension 'w' was varied in the experiment.

$$u = \frac{v_x}{\mathcal{E}} \qquad (6)$$

where v_x is the velocity of either electrons or holes and $\mathcal{E}$ is the electric field in volts/cm. Since the number of thermally generated carriers, n and p in equation 5, is directly proportional to the volume of the active region, any increase in the conductivity, as the wall width cross-sectional region decreases from 95 nm to 20 nm, cannot be attributed to the volume of the semiconductor material, but must be the result of a substantial increase in the carrier mobility and hence velocity

using equation 6. Confirmation of this hypothesized mechanism was obtained with the use of transient time analysis as discussed in section 3.2.

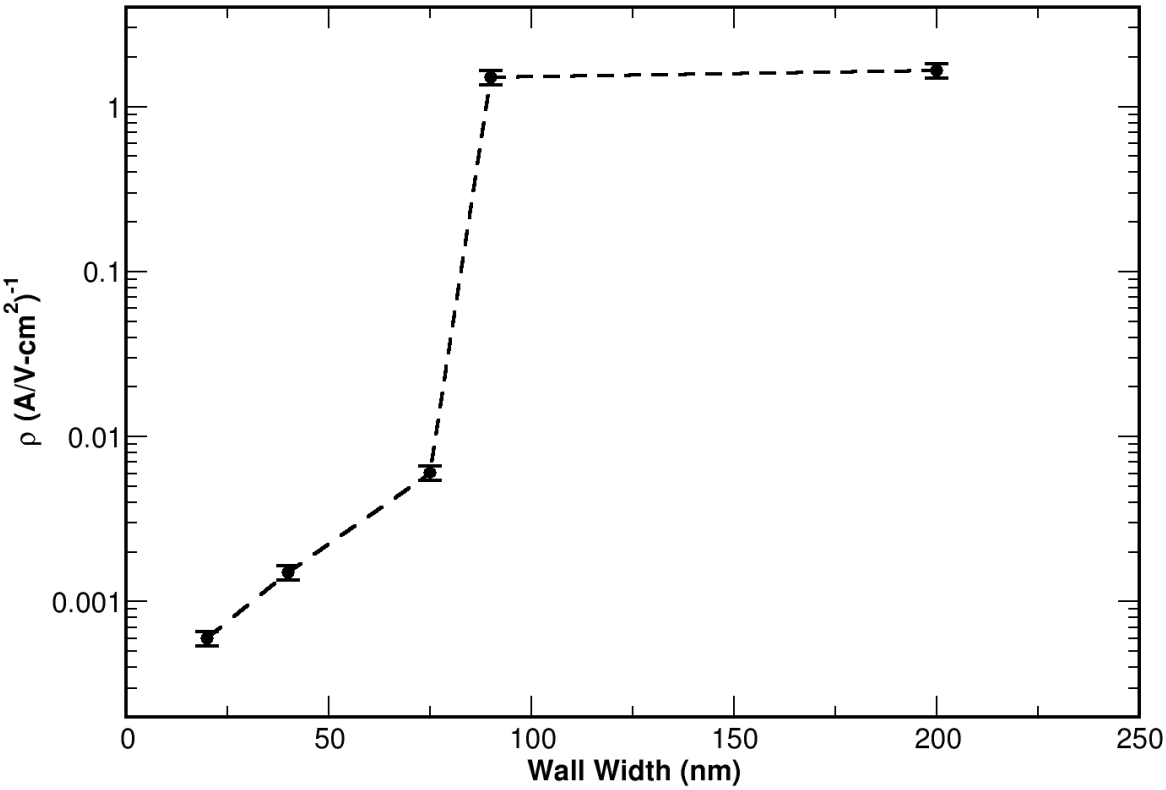

Figure 3.2 Resistivity as a function of active wall width of nanowall structure.

3.3 Photocurrents versus Wall Width Thickness

DC steady state photocurrents were measured using a 365 nm wavelength, 1.132 W/cm^2 argon-ion laser and a 633nm wavelength, 3.96W/cm^2 HeNe laser. The laser beam spot diameter was less than $8\ \mu m$ and was focused within the active region of the electrode spacing covering several wall structures. By using 365 nm and 633 nm wavelengths, a more complete insight into absorption and carrier transport as a function of wall thickness can be achieved. At 365 nm, absorption occurs within the top first $10\ \mathrm{nm}$ of the Si wall structures with heights of $1500\ \mathrm{nm}$. For $633\ \mathrm{nm}$ the total photon absorption extends through the entire wall height. Figures 3.3 and 3.4 show the conductivity versus wall thickness profiles, respectively. As can be noted from the figures, a peak in the conductivity occurs around the 40 nm (physical wall width) samples followed by a decrease around 25 nm width samples. The analysis follows as in section 3.2 and shows that carrier velocities are increasing. The rationale behind this phenomenon can be explained through the effects of strain inside the wall structures that affect the carrier mobilities as the dimensions are reduced, as discussed in Chapter 5.

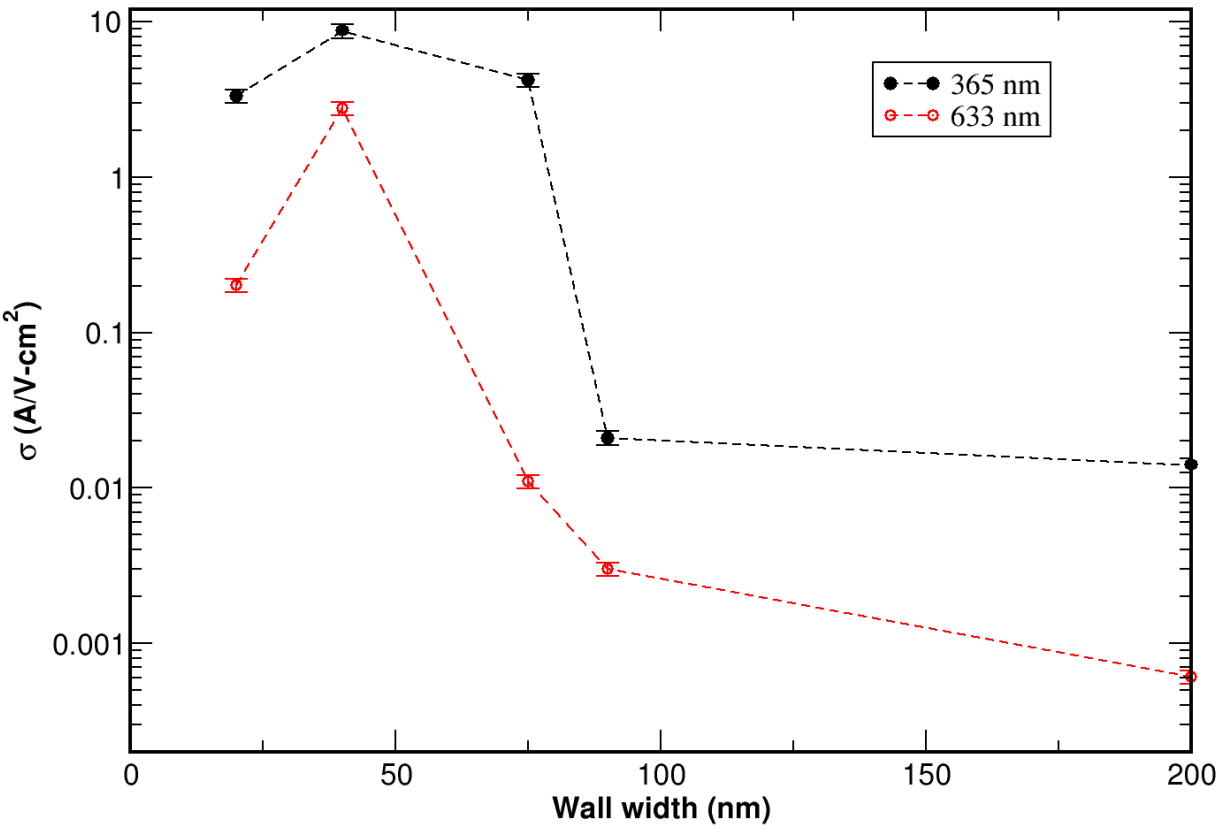

Figure 3.3 Conductivity as a function of active nanowall width for 365 nm and 633 nm wavelengths**.**

3.4 References

1. *An investigation of SiSiO2 interface charges in thermally oxidized (100), (110), (111), and (511) silicon.* **S. Vitkavage, E. A. Irene, H. Z. Massoud.** 5262, s.l. : AIP Publishing Journal of Applied Physics, (1990), Vol. 68. 10.1063/1.347042.

2. **Yang, E. S.** *Microelectronic Devices.* s.l. : McGraw-Hill, Inc., 1988. 0-07-072238-2.

3. **J. R. Haynes and W. Shockley.** 835, s.l. : Phys. Rev., 1951, Vol. 81.

4. **Grundmann, M.** *the Physics of Semiconductors 2nd ed.* Berlin Heidelberg : Springer-Verlag, 2010.

5. *Carrier transport near the Si/SiO2 interface of a MOSFET.* **W. Hansch, T. Vogelsang, R. Kircher, M. Orlowski.** s.l. : Solid-State Electron, 1989, Vol. 32.

6. **W. Hansch, T. Vogelsang, R. Kircher, and M. Orlowski.** 839, s.l. : Solid-State Electron, 1989, Vol. 32.

CHAPTER 4

TRANSIENT TIME RESPONSE MEASUREMENTS

4.1 Description of Experiment

The schematic of the pulsed carrier transport experiment is shown in Figure 4.1. This setup is based on a modified version of the Haynes-Shockley experiment (1). This measurement provides an unambiguous direct measure of the actual transit time of electrons and holes through the channel. When a narrow pulse of light strikes the wall structured active region of the device near the left electrode as shown in Figure 4.1, equal number of electrons and holes are generated, and are then subjected to diffusion and drift forces in the presence of an electric field. Based on the experimental configuration, the electrons will be rapidly collected near the positively biased electrode and the holes will have to travel the entire channel to the negatively biased electrode. From the measured time response signal profile at the opposite electrode, the hole transient time limited carrier velocity can be determined, provided the carrier lifetime is greater than the total transit time (2). If the optical pulse of

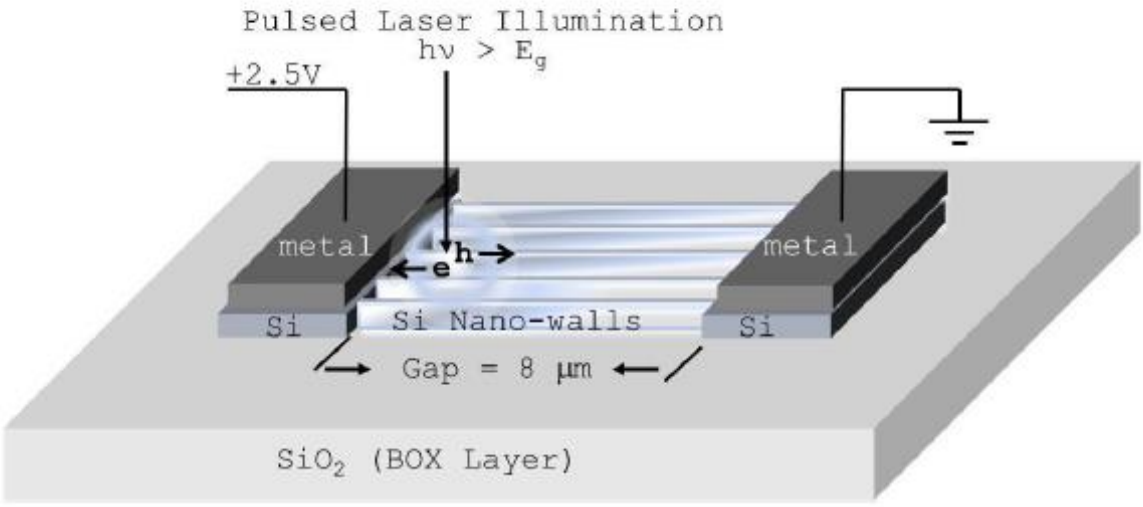

Figure 4.1 Schematic of modified Haynes-Shockley experiment.

light strikes near the opposite electrode, the holes will be rapidly collected and the electrons would have to transit through the channel, thus the measured signal at the opposite electrode would be electron transit time limited. The pulsed response measurements were taken using a $150 - fs$ duration excitation at λ=$400\ nm$ from a cw modelocked $Ti{:}\,Al_2O_3$ laser (doubled for the short wavelength, $0.2\ mW$ average power at a $77\ MHz$ repetition rate). The wall structured MSM devices were probe tested using an $18\ GHz$ probe and a high-speed digital sampling oscilloscope with an approximately $1\ ps$ resolution capability. The laser spot size was $1\ \mu m$ in diameter and the electrode gaps were $8\ \mu m$. Normal incidence was used for the experiment. The time response measurements were taken for low electric field strengths $3x10^3\ \ V/cm$, (2.5 V across $8\ \mu m$ gap) thus avoiding velocity saturation. Before the experimental data

and analysis are provided, it is useful to review the three primary factors that can impact the carrier transport through a semiconductor region. These factors are:

- Field dependent velocity of carriers through the active region. At high E-fields, the velocities of both electrons and holes in Si saturate at about $1x10^7\ cm/s$ (3), provided the field within the electrodes exceeds the saturation value for most of its length, we can assume that the carriers move with an average velocity drift. Velocity saturation is not an issue in our experiment since the applied field is much lower than what is required for saturation.
- Diffusion of carriers in the active region. The time it takes for carriers to diffuse a distance d is $\tau_{diff} = d^2/2D$ where D is the carrier diffusion coefficient. The diffusion of carriers becomes a two dimensional process as the thickness of the Si wall-structures is reduced and carriers are physically constricted in movement by the Si/SiO2 interfaces from all sides.
- Junction and parasitic capacitance effects. A metal semiconductor junction under reverse bias exhibits a voltage-dependent capacitance caused by the variation in stored charge at the junction represented by the relation

$$C_j = \left(A/2\right)\sqrt{2e\epsilon_o\epsilon_r N_d/V} \qquad (1)$$

where A is the junction cross-sectional area, N_d is the ionized donor density, ϵ_r is the dielectric constant, and V is the junction voltage. This capacitance is usually quite small for MSM device structures as a result of their planar electrode design. There are also parasitic circuit capacitances associated with the probing and

cabling that usually dominate the electrical response as well as the limiting response of the electronics. For this study, all film devices have an identical circuit limitation.

Figure 4.1 shows the bias polarity of our experiment in which the left electrode polarity is positive and the right electrode is ground. With this bias configuration once a pulse of light with a spot size <1 lm, as in the case of our experiment, strikes within the active region, the holes travel towards the right electrode and the electrons travel in the opposite direction towards the left electrode. From the experimental results of the time response measurements for 200 nm, 95 nm, 40 nm, and 20 nm thick wall devices for both electron and hole dominated signals the rise times were found. From a first pass, as the thickness of the wall-channels is decreased, the time response signal decays faster. In particular, in the case of the 40 nm and 20 nm thick walls, the signal decays over an order of magnitude faster than the 200 nm sample for both electrons and holes. The rise time of the signals is an important parameter, since it directly provides the carrier transit time (4). The transit time (td) is defined as the time-lapse from the moment when the pulse of light strikes one end of the active region of the MSM, near one electrode, and the moment when the photogenerated carrier signal is detected at the opposite electrode. From the rise time data, we can determine the carrier mobilities as a function of wall thickness as follows (4).

4.2 Data Analysis

First from the experimental time response measurements, we can calculate the average carrier velocities by applying the given relation

$$V_{Carrier-Velocity} = \frac{(Electrode\ gap)}{t_d}\ (\frac{cm}{s}) \qquad (2)$$

where t_d is the average time it takes for the pulsed carrier signal to cross the electrode gap distance. The pulse travels in the presence of a field and expands from its originating point due to diffusion (5). In this case, we are ignoring the RC time delay that the pulsed signal experiences once it reaches the edge of the depletion region near the electrodes since the widths of the depletion regions are very small in the sub-micron range compared to the electrode gap which is 8 um in length. By definition, the average carrier mobility can be written as

$$\mu_{avg} = \frac{v_{Carrier-Velocity}}{V_{bias}/(Electrode\ gap)} \qquad (3)$$

where V_{bias} is the external bias applied to the electrodes.

Figure 4.2 shows a plot of average field dependent electron and hole limited mobility values using experimental values of rise time, t_d, and the above expression as a function of wall thickness.

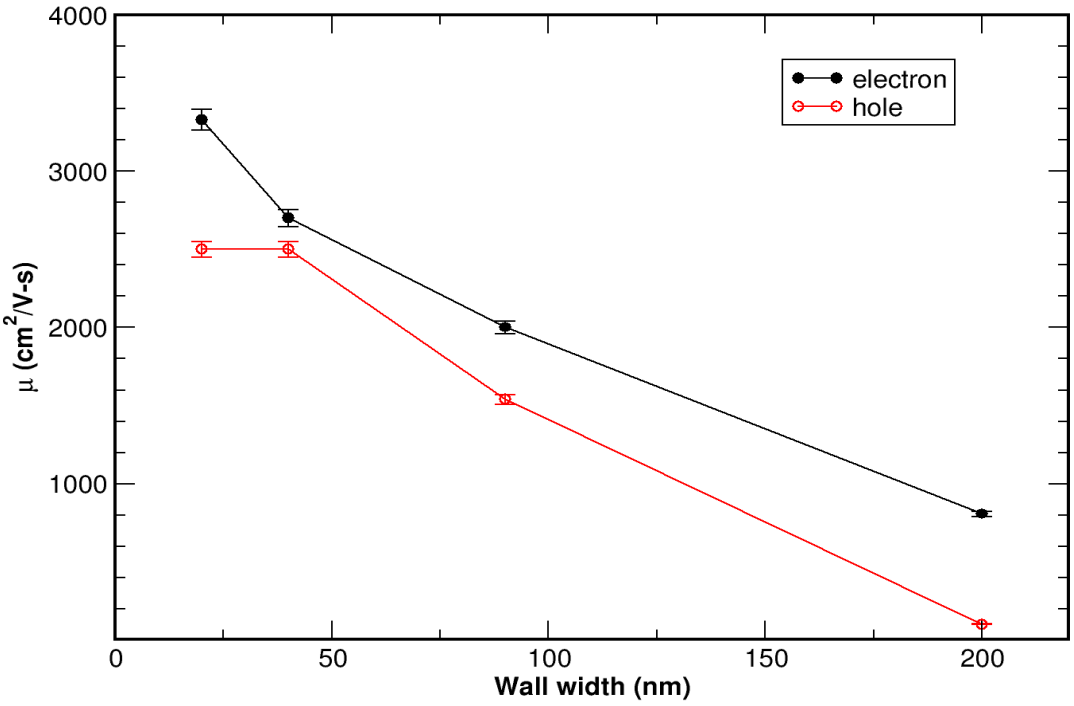

Figure 4.2 Carrier mobility values calculated from direct measure of rise time as a function of wall thickness.

We know that the carrier transport of electrons and holes in the thickest wall sample (200 nm) is essentially similar to the transport properties in bulk silicon. However, we observe a considerable increase in low field dependent mobility values below 75 nm wall thicknesses. Recall the fact that we actually have much narrower effective cross-sectional regions from which carriers propagate due to the repulsive nature of the boundary at the Si/SiO_2 interface, and the carrier profile tends to peak a certain distance away from the interface close to the center of the wall structures (6). At these nanoscales, we must account for the

strain effects, which include the reversal splitting of light- and heavy-hole bands as well as the decrease of conduction-band effective mass by reduced Si bandgap energy. These strain effects are formulated in our microscopic model for explaining the experimentally observed enhancements in both conduction- and valence-band mobilities with reduced Si wall thickness, i.e., consider the case where the hole mobility is given by

$$\mu_h = e\tau_h / m_h^* \qquad (4)$$

where

$$1/m_{ij}^* = (1/\hbar)\left(\partial^2 E(k)/\partial k_i \partial k_j\right). \qquad (5)$$

The narrower light-hole band dominating the transport can have a significant enhancement on the overall mobility which is consistent with our experimental result. Specifically, the enhancements of the valence-band and conduction-band mobilities are found to be associated with different aspects of physical mechanisms. The role of the biaxial strain buffering depth is elucidated and its importance to the scaling relations of wall-thickness is reproduced theoretically. A detailed theoretical model is described in Chapter 5 which explains our experimental results in a comprehensive manner.

4.3 References

1. **Shockley, J. R. Haynes and W.** 835, s.l. : Phys. Rev., 1951, Vol. 81.

2. **Streetman, B. G.** *Solid State Electronic Devices.* Englewood Cliffs, N. J. 07632 : Prentice-Hall, Inc., 1980. ISBN: 0-13-822171-5.

3. **Yang, E. S.** *Microelectronic Devices.* s.l. : McGraw-Hill, Inc., 1988. 0-07-072238-2.

4. **Grundmann, M.** *The Physics of Semiconductor 2nd ed.* Berlin Heidelberg : Springer-Verlag, 2010.

5. **Wang, Shyh.** *Fundamentals of Semiconductor Theory and Device Physics.* Englewood Cliffs : Prentice-Hall, Inc., 1989. ISBN 0-13-344409-0.

6. *Carrier transport near the Si/SiO2 interface of a MOSFET.* **W. Hansch, T. Vogelsang, R. Kircher, M. Orlowski.** s.l. : Solid-State Electron, 1989, Vol. 32.

Chapter 5

THEORY AND ANALYSIS

5.1 Crystal band structure

The periodicity of the potential of the crystal lattice is the underlying cause of the difference between carrier propagation in an ideal homogenous, isotropic media such as a vacuum and in a crystal lattice structure. The periodicity of the lattice is incorporated into the electron dynamics via the potential function in the Shrödinger equation. The time independent one dimensional version of this equation utilizing the one-electron approximation leads to a description of allowed electron energies and quantum states for a crystal (1). The one-electron approximation is reasonable since the forces exerted on a single electron by other charges average to zero over any reasonable time length and therefore electrons only experience forces due to the lattice potential (1).

The simplest one-dimensional periodic potential is shown in Figure 5.1.

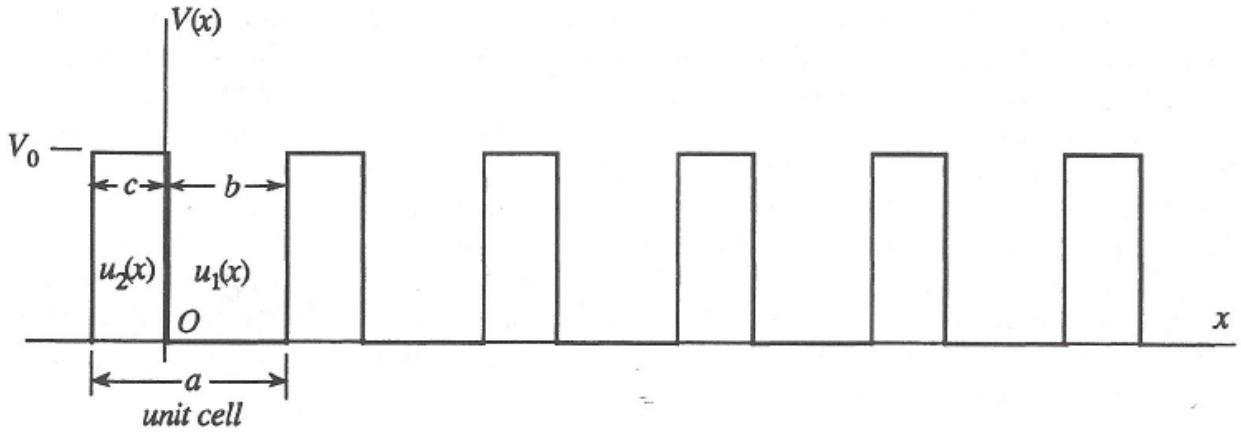

Figure 5.1 The periodic potential used by Kronig-Penney in their one-dimensional model *(1)*.

Kronig and Penney applied the Bloch form of the wave function, $\Psi(\mathrm{x}) = e^{ikx}u(x)$, to the Shrödinger equation

$$\frac{d^2\Psi}{dx^2} + \frac{2m}{\hbar^2}[\mathcal{E} - V(x)]\Psi(\mathrm{x}) = 0. \qquad (1)$$

The wave equation, $u(x)$, must satisfy the one dimensional Shrödinger equation for each potential in the unit cell. Substitution of $\Psi(\mathrm{x})$ results in the following second order differential equation:

$$\frac{d^2u}{dx^2} + 2ik\frac{du}{dx} - \left(k^2 - \alpha^2 + \frac{2mV(x)}{\hbar^2}\right)u(x) = 0 \qquad (2)$$

where

$$\alpha^2 = 2m\mathcal{E}/\hbar^2, \qquad (3)$$

m is the mass of an electron, $\mathcal{E}$ is the energy of an electron, k is the wavenumber, $\hbar$ is Planck's constant divided by 2π.

Since the potential exists in piecewise form, the equation must be solved for each region:

$$\frac{d^2u_1}{dx^2} + 2ik\frac{du_1}{dx} - (k^2 - \alpha^2)\mu_1(x) = 0 \qquad (4)$$

$$\frac{d^2u_2}{dx^2} + 2ik\frac{du_2}{dx} - (k^2 - \beta^2)\mu_2(x) = 0 \qquad (5)$$

Where

$$\beta^2 = 2m(\mathcal{E} - V_o)/\hbar^2.$$

The solution to these equations are:

$$u_1(x) = Ae^{i(\alpha-k)x} + Be^{-i(\alpha+k)x}, \qquad (0 < x < b) \qquad (6)$$

$$u_2(x) = Ce^{i(\alpha-k)x} + De^{-i(\alpha+k)x}, \qquad (-c < x < 0) \qquad (7)$$

The constants, A, B, C, and D can be found by requiring the wave functions and their derivatives be continuous at boundaries $x = b$ and $x = c$. These requirements result in the following dispersion relation (1):

$$\left[1 + \frac{V_o^2}{4\mathcal{E}(\mathcal{E}-V_0)}sin^2\beta c\right]^{1/2}\cos(\alpha b - \delta) = coska(6), (\mathcal{E} > V_o) \qquad (8)$$

$$\left[1+\frac{V_o^2}{4\mathcal{E}(\mathcal{E}-V_0)}sinh^2\beta c\right]^{1/2}\cos(\alpha b-\delta')=coska(6),\ (0<\mathcal{E}<V_o) \quad (9)$$

Where

a is the lattice constant $b+c$ and

$$tan\delta=-\frac{\alpha^2+\beta^2}{2\alpha\beta}tan\beta c \quad (10)$$

$$tan\delta'=\frac{\gamma^2-\alpha^2}{2\alpha\gamma}tanh\gamma c \quad (11)$$

$$\alpha^2-\beta^2=\alpha^2+\gamma^2=2mV_o/\hbar^2 \quad (12)$$

These equations, which constitute the dispersion relation resulting from the use of the 1D time independent Shrödinger equation, place restrictions on values of $\alpha b-\delta$ where quantum states of the system cannot exist. Since this is related to the electron energy through equation 3, this states that there are energies where no quantum states can exist. Since energy is given in terms of the parameter α, choosing a value of α determines both energy and crystal momentum $(\hbar k)$ by equations 8 and 9. Doing so for many such α's generates the following energy versus wavenumber, or $\mathcal{E}$ versus k diagram as shown in Figure 5.2.

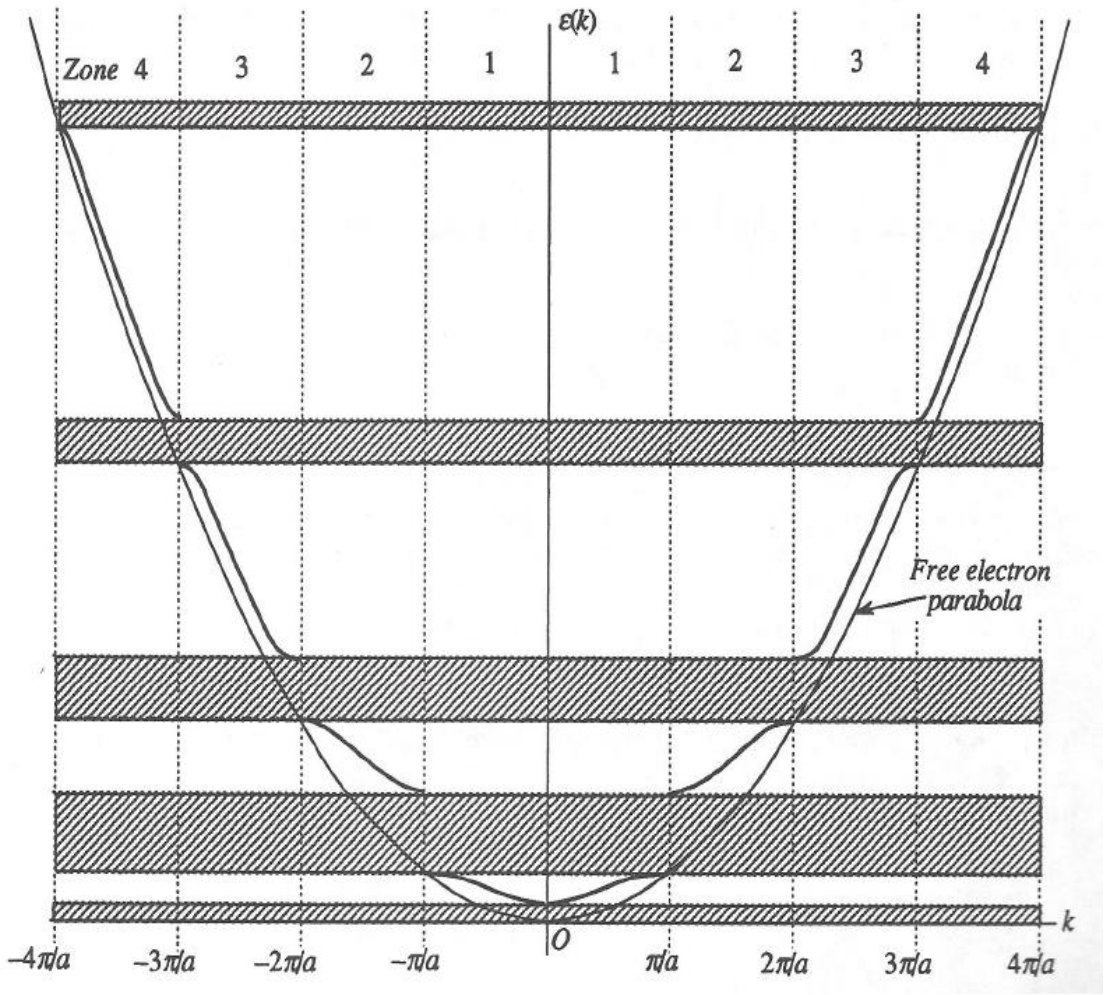

Figure 5.2 Dispersion relation for the single electron model, the Kronig- Penney periodic potential, showing energy vs crystal momentum (1).

The dispersion diagram is typically shown in a reduced zone format as shown in Figure 5.3. As shown in Figure 5.2, the band edges are defined for $k = n\frac{\pi}{a}$, $n = 0, 1, 2, \ldots$. These values for the wavenumber also satisfy the Bragg condition and the area within the band define the Brillouin zones (1).

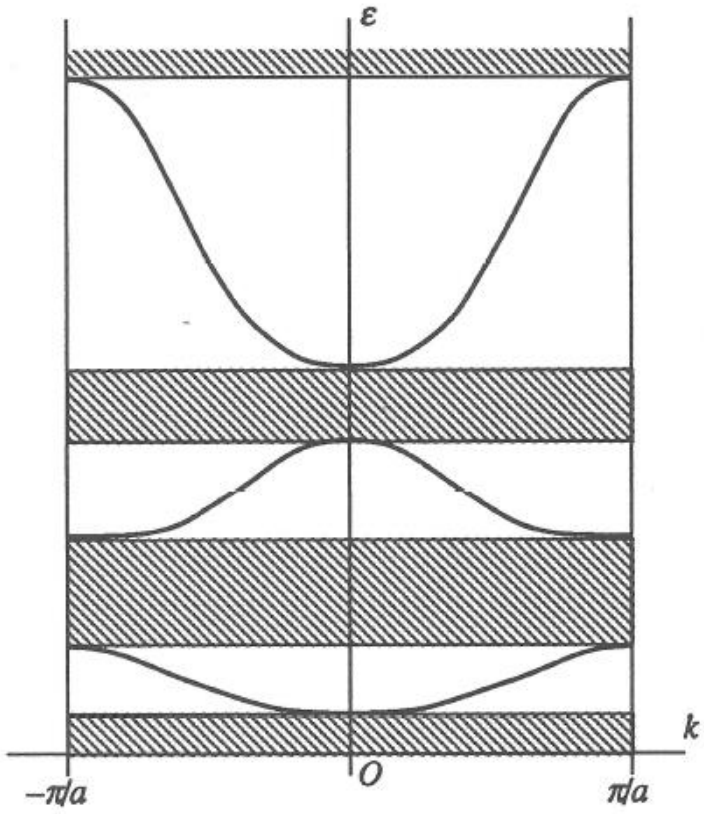

Figure 5.3 Reduced zone format for energy-momentum band diagram of Figure 5.2 *(1)*.

The dispersion relation for a free electron is:

$$\mathcal{E} = \hbar\omega = \frac{\hbar^2 k^2}{2m}. \qquad (13)$$

The energy of the particle moves with the group velocity $d\omega/dk$ as follows:

$$\frac{dv_g}{dt} = \frac{d}{dt}\left(\frac{d\omega}{dk}\right) = \frac{d}{dk}\left(\frac{d\omega}{dk}\right)\frac{dk}{dt} = \frac{1}{\hbar^2}\frac{d^2\mathcal{E}}{dk^2}\frac{d(\hbar k)}{dt} \qquad (14)$$

And using classical mechanics the work done on an electron can be expressed as follows (1):

$$dW_e = F_e dx = F_e v_g dt = F_e \frac{d\omega}{dk} dt, \qquad (15)$$

$$dW_e = d\mathcal{E} = \frac{d\mathcal{E}}{dk} dk = \hbar \frac{d\omega}{dk} dk. \qquad (16)$$

When these are equated:

$$F_e = \frac{d(\hbar k)}{dt} \qquad (17)$$

and when this is substituted into equation 14:

$$\frac{dv_g}{dt} = \frac{1}{\hbar^2} \frac{d^2\mathcal{E}}{dk^2} F_e = \frac{F_e}{m^*} \qquad (18)$$

where

$$m^* = \frac{\hbar^2}{d^2\mathcal{E}/dk^2} \, . \qquad (19)$$

This result can be generalized to the Kronig-Penney periodic potential in that the effective mass is a function of the curvature of the energy band functions. Additionally the effective mass is a result of the periodic lattice potential and varies with crystal momentum. In this model, the electron is effectively a free particle that responds to external forces but with a modified mass. Further, at the top of the band, the curvature is negative, suggesting a negative mass. Under the influence of an electric field in the x-direction, this would produce a positive acceleration along the x-direction. Therefore, a positive sign is assigned to the

charge and the mass rather than a negative charge and negative mass, and it is called a hole.

The Kronig-Penney model can be extended to three dimensions, the effective mass then becomes a tensor defining a unique effective mass for each direction in a crystal, and complex energy band structures result such as that for silicon as shown in Figure 5.8 below. Additionally, band diagrams calculated from an analysis of atoms arranged in a diamond lattice as the interatomic spacing is reduced from infinity as shown in Figure 5.5 become three dimensional in nature, as shown in Figure 5.4 with energy band features and effective masses dependent upon direction in the crystal. Further, the effective mass used in calculations of current conduction based on mobilities must incorporate an average mobility modified by mobilities weighted by respective carrier concentrations. Experimentally, the mobilities were calculated based on carrier velocities from which the ratio of carrier lifetime to effective mass can be calculated as:

$$\mu = \frac{v_c}{E} = \frac{e\tau}{m^*} \qquad (20)$$

where μ is the mobility of a carrier (electron or hole), v_c is the carrier speed, E is the electric field, e is the electronic charge, τ is the carrier lifetime, and m^* is the carrier effective mass.

Theoretically the carrier mobilities are calculated based on band degeneracy with averaged weighted mobilities, modified carrier lifetimes, and

modified effective masses as shown below. The two are plotted together in Figure 5.13.

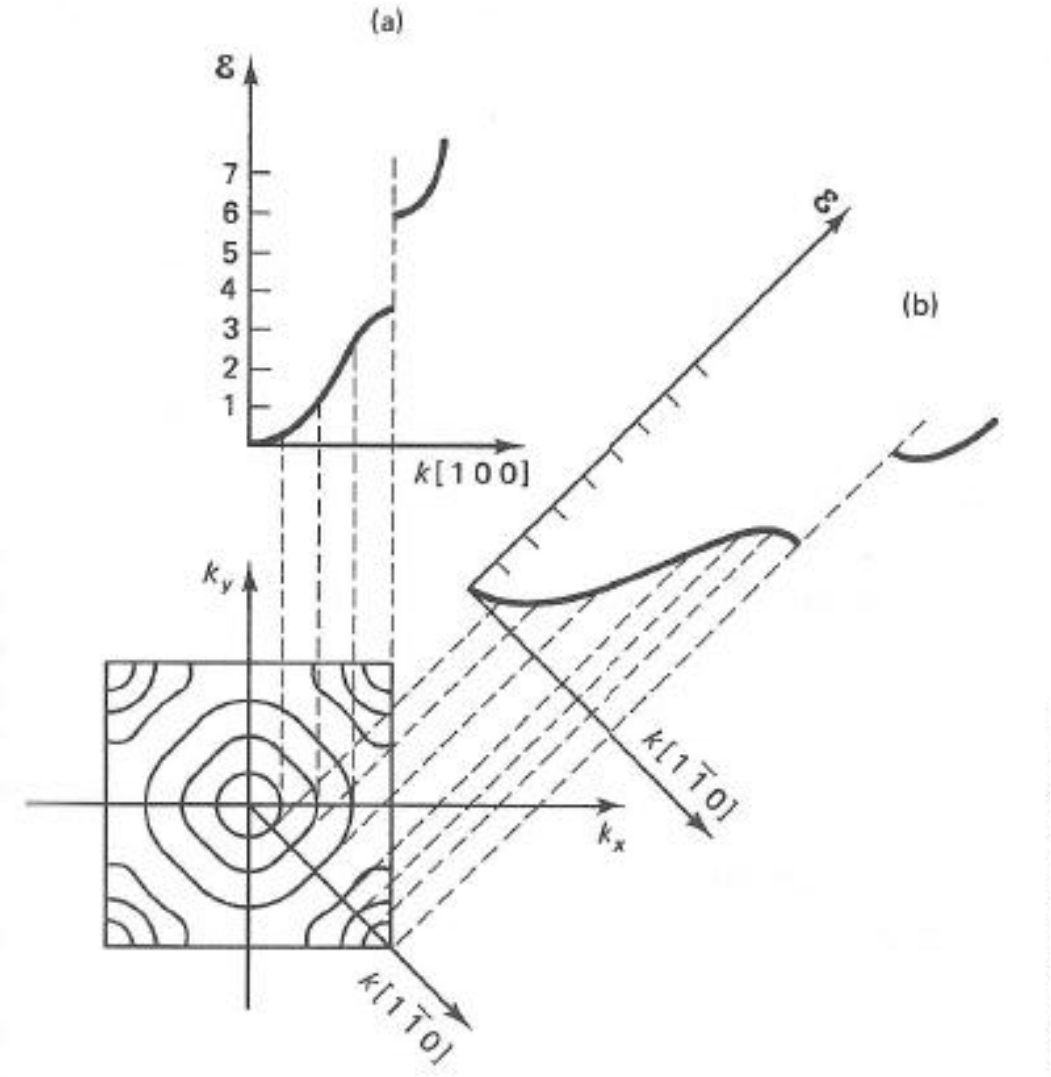

Figure 5.4 Energy versus wave vector from plots of constant energy contours along various crystal directions *(2)*.

5.2 Theoretical development of deformation potentials

The above analysis applies to a lattice in equilibrium at lattice constant 'a' in Figure 5.5. The effect of the deformation of the crystal lattice by external forces (stress) such as acoustic waves on carrier mobilities (also termed lattice scattering, the dominant scattering mechanism in this experiment since samples are lightly doped) in non-polar crystals was investigated by Bardeen and Shockley (3). Their objective was to determine shifts in the energy band edge of both the conduction and valence bands associated with dilations of the crystal produced by thermal vibrations. At the time this experiment was conducted, direct calculations of energy bands from first principles was not possible. Therefore the theory was confirmed from experimental data since quantities calculated from the mobilities would be definitively related to effects produced by external forces such as acoustic waves, pressure and temperature.

In their paper they estimated the interaction between charge carriers and acoustical waves in non-polar crystals subject to the following assumptions

$$\lambda_{e^-} \gg a \qquad (21)$$

$$E_{phonon} \ll kT \qquad (22)$$

$$E_{phonon} \ll E_{e^-} \qquad (23)$$

where λ_{e^-} is the wavelength of a room temperature electron, $7x10^{-7}$ cm, and is large compared to the lattice constant a, E_{phonon} is much less than kT (.0259 eV), and additionally E_{phonon}, the phonon energy is much less than the energy of a thermal electron (E_{e^-}). Under these assumptions the acoustical phonons

can be treated by classical statistical methods (3). The authors extended the method of effective mass to gradual shifts in energy bands resulting from deformations of the crystal lattice and coined the term ‘deformation potentials’ to refer to the effective potential which corresponds to the position of the energy band edge as it is affected by the gradually varying dilation of the acoustic wave. The deformation potential is used in the formulation of the relaxation time for an electron scattered from an initial state to a final state, from which the mean free path and mobility are calculated.

In Fig. 5.5 is shown a typical energy band diagram for a non-polar crystal such as in this case diamond, and in general for silicon, that results when atoms with discrete energy levels are brought close enough together that individual electronic waves interact and form energy bands as a result of a periodic lattice. A perturbing influence such as an applied electric field causes the conduction and valence bands to move in the same direction and results in no change to the energy gap since $E_g = E_c - E_v$. A small dilation or contraction of the lattice constant resulting from a longitudinal wave however, causes the energy band structure as shown in Fig. 5.5 to change the separation energy between the conduction band and the valence band. Ultimately this perturbation will affect carrier mobilities.

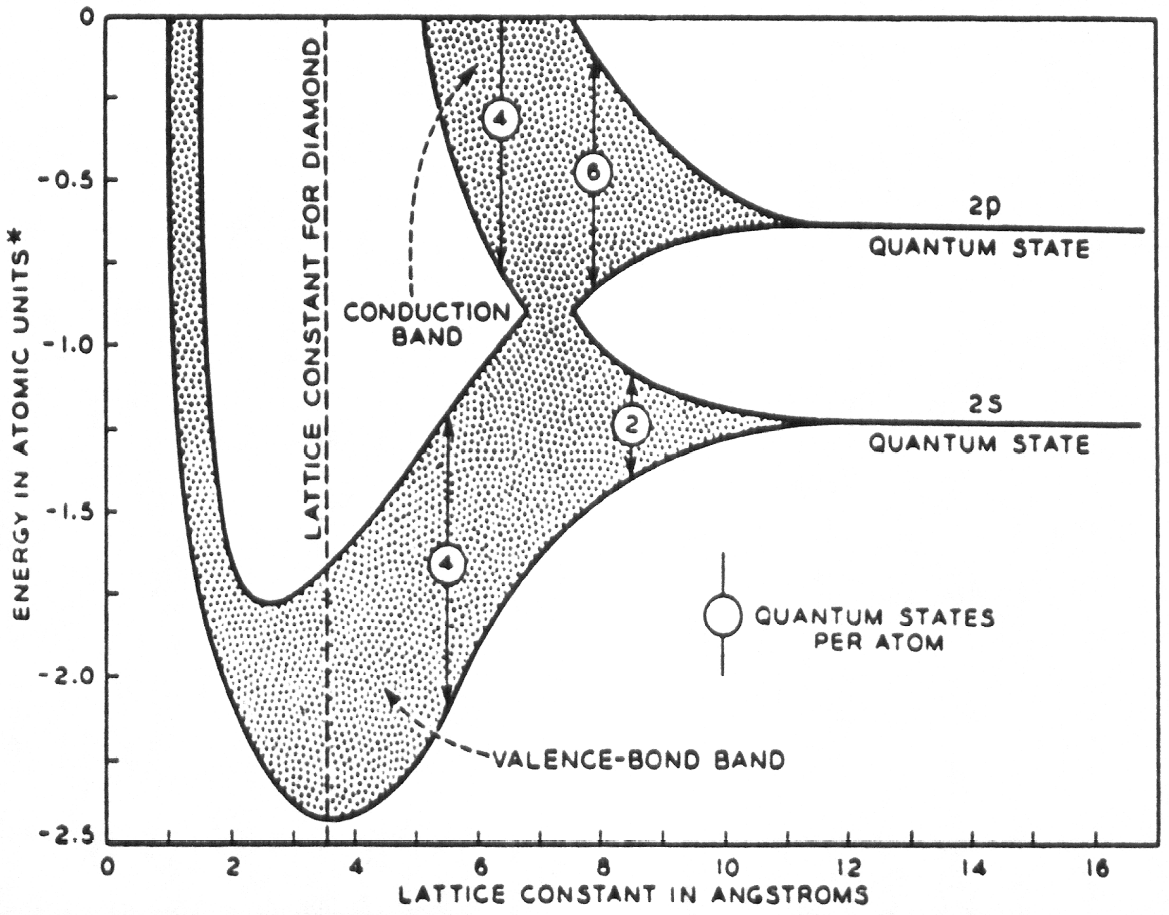

Figure 5.5 Energy band diagram for diamond versus lattice spacing (12).

As defined in the paper, the dilation or contraction of the position of the conduction band is a result of strain from, in this case, the stress of acoustic lattice waves, and is expressed as,

$$E(\epsilon_{ij}) = E_0 + E_1\Delta \qquad (24)$$

for the conduction band edges E_c or E_v where

$$\Delta = \epsilon_{11} + \epsilon_{22} + \epsilon_{33} \qquad (25)$$

since off diagonal strains are zero due to symmetry arguments. Likewise, the energy expressed in terms of the crystal momentum **P** will be

$$E(P, \epsilon_{ij}) = E_0 + \sum_{ij} \epsilon_{ij} E_{ij}(P). \qquad (26)$$

When E_{ij} is expanded about small crystal momentum P, after neglecting terms in P^2 x strains, the following results:

$$E(P, \epsilon_{ij}) = E_o(P) + E_1\Delta. \qquad (27)$$

This result gives the energy for a state with a particular **P** as a result of strain with $\Delta = \epsilon_{11} + \epsilon_{22} + \epsilon_{33}$, where off diagonal elements of the strain are zero as a result of symmetry. Bardeen and Shockley then show that in a strained lattice the crystal momentum **P** having a factor exp(i**P**·**r**) will have energy

$$E(P, \epsilon_{ij}) = E_o(P) + \sum_{ij} \epsilon_{ij} E_{ij}(P). \qquad (28)$$

When P is small compared to the Brillouin zone, the energy $\mathrm{E_{ij}}$ can be expanded in a power series resulting in the following:

$$E(P, \epsilon_{ij}) = E_0 + E_1\Delta + terms\ in\ P^2. \qquad (29)$$

The second term, $E_1\Delta$, is the deformation potential in Bardeen-Shockley's work (3) and is shown to be equivalent to a perturbing potential (V_p) resulting from lattice waves (phonons) that couple to electrons resulting in scattering from momentum state P to P' in accordance with Fermi's Golden Rule and subject to the selection rule

$$P' = P \pm \hbar\mathbf{k} \pm \hbar\mathbf{K} \qquad (30)$$

in the matrix

$$M(\boldsymbol{P}, \boldsymbol{P'}) = \int \Psi^*(P')V_p\Psi(P)d\tau. \qquad (31)$$

that determines the scattering probably from state P to P', where ψ is the modified wave function at the band edge, modified by an amplitude function derived from the solution to Shrodinger's equation using the deformation potential.

A distortion is mathematically expressed in terms of a displacement of the atom centered at the lattice position $\boldsymbol{r}_n$ as

$$\delta\boldsymbol{R}_n = \delta R(\boldsymbol{r}_n). \qquad (32)$$

In their work, it is shown that $E_1\Delta$ is approximately equivalent to V_p and therefore, using $E_1\Delta$ for V_p in equation 31 the matrix element can be evaluated.

The displacement of an atom at $\boldsymbol{R_n}$ as a result of a phonon is

$$\delta \boldsymbol{R} = N^{1/2} \boldsymbol{l}_k (a_k exp(i\boldsymbol{k} \cdot \boldsymbol{R_n}) + a_k^* \exp(-i\boldsymbol{k} \cdot \boldsymbol{R_n})) \qquad (33)$$

Where $\boldsymbol{l}_k$ is a unit vector in the direction of the displacement and N is the number density of atoms in a unit volume, and $\boldsymbol{k}$ is the wavevector of phonons.

The divergence of the displacement is the dilation of the lattice as follows:

$$\Delta(\boldsymbol{r}) = div \delta \boldsymbol{R}(\boldsymbol{r}) = iN^{\frac{-1}{2}} (\boldsymbol{k} \cdot \boldsymbol{l_k}) [a_k \exp(i\boldsymbol{k} \cdot \boldsymbol{r}) - a_{\boldsymbol{k}}^* \exp(-i\boldsymbol{k} \cdot \boldsymbol{r})] \quad (34)$$

where $\Delta(\boldsymbol{r})$ is the lattice deformation and $\boldsymbol{r}$ is the vector direction to an atom in the crystal. a_k is the amplitude of the lattice wave, the magnitude of such a wave is:

$$|a_k|^2 = k_o T / 2Mk^2 c_l^2 \qquad (35)$$

where k_0 is Boltzmann's constant, M is the mass of an atom, and c_l is the velocity of a longitudinal lattice wave. When the operation in equation 31 is conducted using equation 34, it is found that

$$\left|M(\boldsymbol{P}, \boldsymbol{P'})\right|^2 = E_1^2 k_0 T / 2NMc_l^2 = E_1^2 k_0 T / 2\rho c_l^2 \qquad (36)$$

Where $\rho = NM$ and the elastic constant can be substituted for $c_{ii} = \rho c_l^2$. The reciprocal for the relaxation time can be found (2; 3)by performing the following integration:

$$1/\tau = (m_e P / \pi \hbar^4) \int_0^{\pi} \left|M(\boldsymbol{P}, \boldsymbol{P'})\right|^2 (1 - \cos\theta) sin\theta d\theta \qquad (37)$$

where θ is the angle between **P** and **P'**, resulting in

$$1/\tau = m_e P E_1^2 k_o T/\pi\hbar^4 c_{ii}, \qquad (38)$$

resulting in a mean free path of

$$1/l = 1/\tau v = m_e^2 E_1^2 k_o T/\pi\hbar^4 c_{ii}. \qquad (39)$$

The mobility is found (2; 3)

$$\mu = \frac{q\bar{\tau}}{m} \qquad (40)$$

and

$$\bar{\tau} = \frac{\langle v^2 \tau(v)\rangle}{\langle v^2\rangle} \qquad (41)$$

so that the mobility is

$$\mu = \frac{4el}{3(2\pi m_e k_0 T)^{\frac{1}{2}}} = \frac{2(2\pi)^{\frac{1}{2}} e\hbar^4 c_{ii}}{3m_e^{5/2}(k_0 T)^{3/2} E_1^2}. \qquad (42)$$

and culminates in the same result developed by Wang (2) utilizing reflection and transmission coefficients associated with the perturbed band structure resulting from the deformation potentials.

This investigation clearly shows the effect of strain on carrier mobilities, Bardeen and Shockley used this result to calculate the change in band gap of materials as a result of strain for both electrons and holes from a number of stressors such as temperature and pressure from measurements of carrier mobilities. Our objective on the other hand (4), was to predict carrier mobilities as a result of strain produced from the lattice mismatch at the interface between

silicon dioxide (SiO_2) and the crystalline silicon channel as shown in Figure 5.6. The stress at this interface is not trivial, measurements of the stress at the Si/SiO_2 interface by Borden showed stress approaching 80,000 psi (5). The strain producing stress alters the band structure of the silicon causing changes to the carrier effective mass, carrier lifetimes and mean free paths, and splitting of valence bands, the total effects of which are encompassed in the following theoretical analysis.

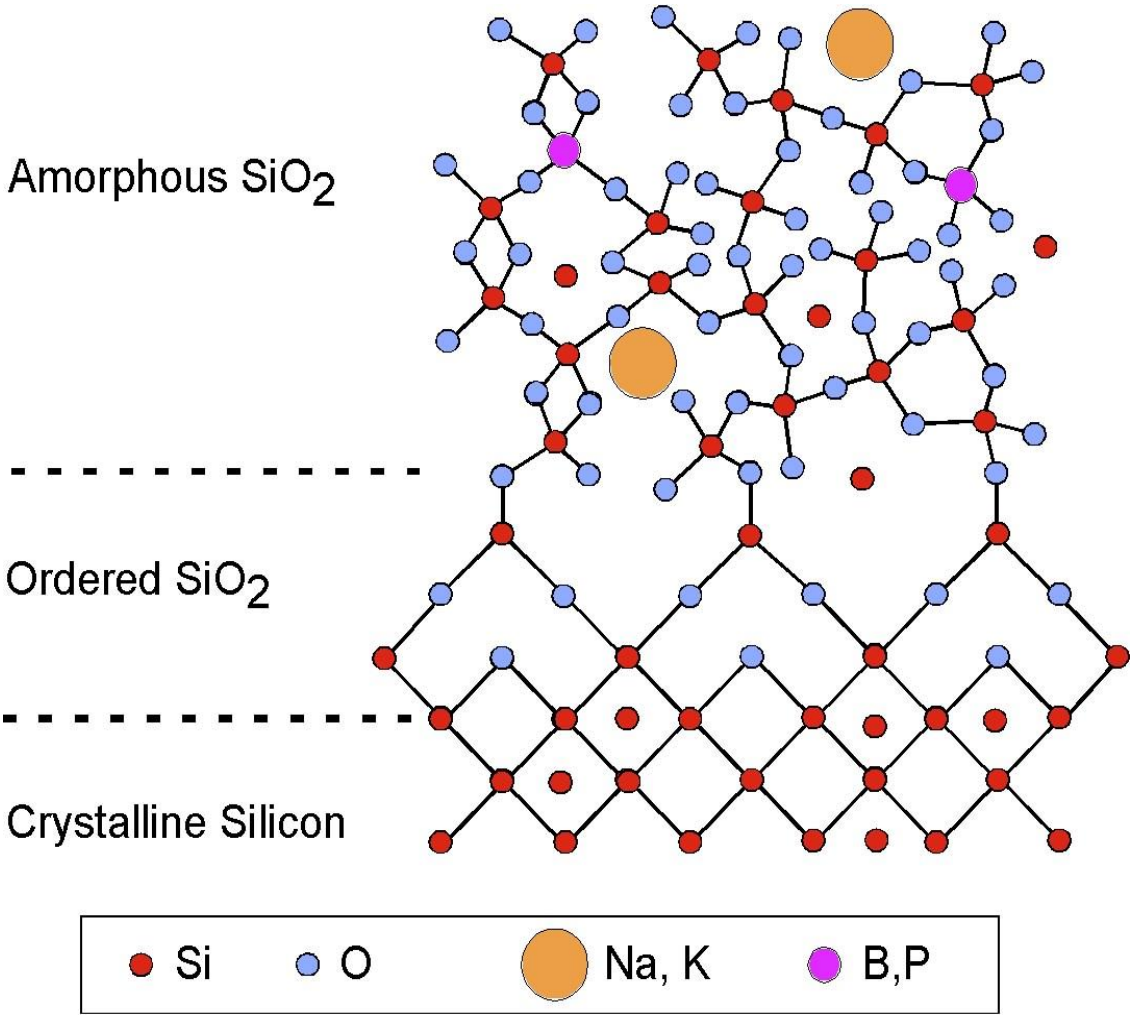

Figure 5.6 Transition from ordered crystalline silicon at bottom to amorphous SiO2 at top, including transition period and inclusion of impurities.

5.3 Strain Effects Modeling to Explain the Rise in Electron and Hole Mobility (4)

Figures 5.7 and 5.8 represent the thickest wall channels, and Figures 5.10 and 5.11 represent the thinnest wall channels. Note that the associated *E-k* diagrams of Figures 5.9 and 5.12 represent the center regions of the wall channel structures where the carriers flow through.

Figure 5.7 SEM image of single 200 nm wall.

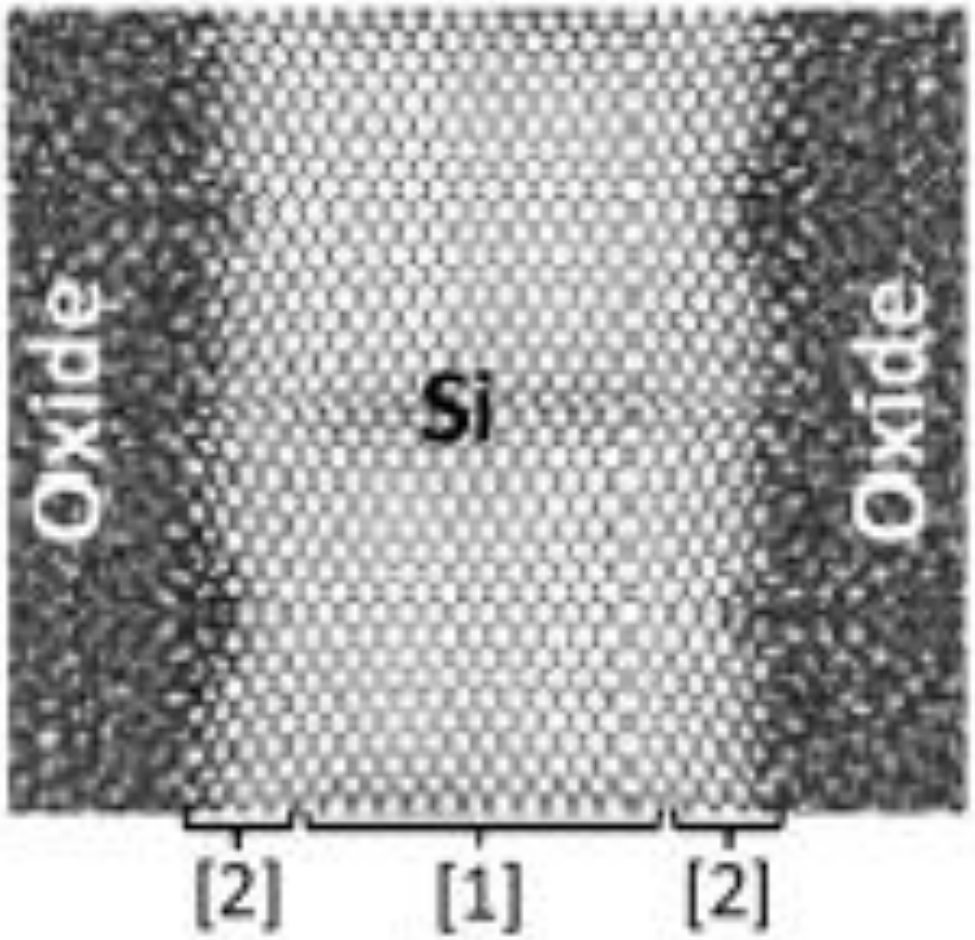

Figure 5.8 Artist's depiction of Si and O atoms shown by light and dark gray spheres, respectively. Region -[1] is unstrained while region -[2] is strained.

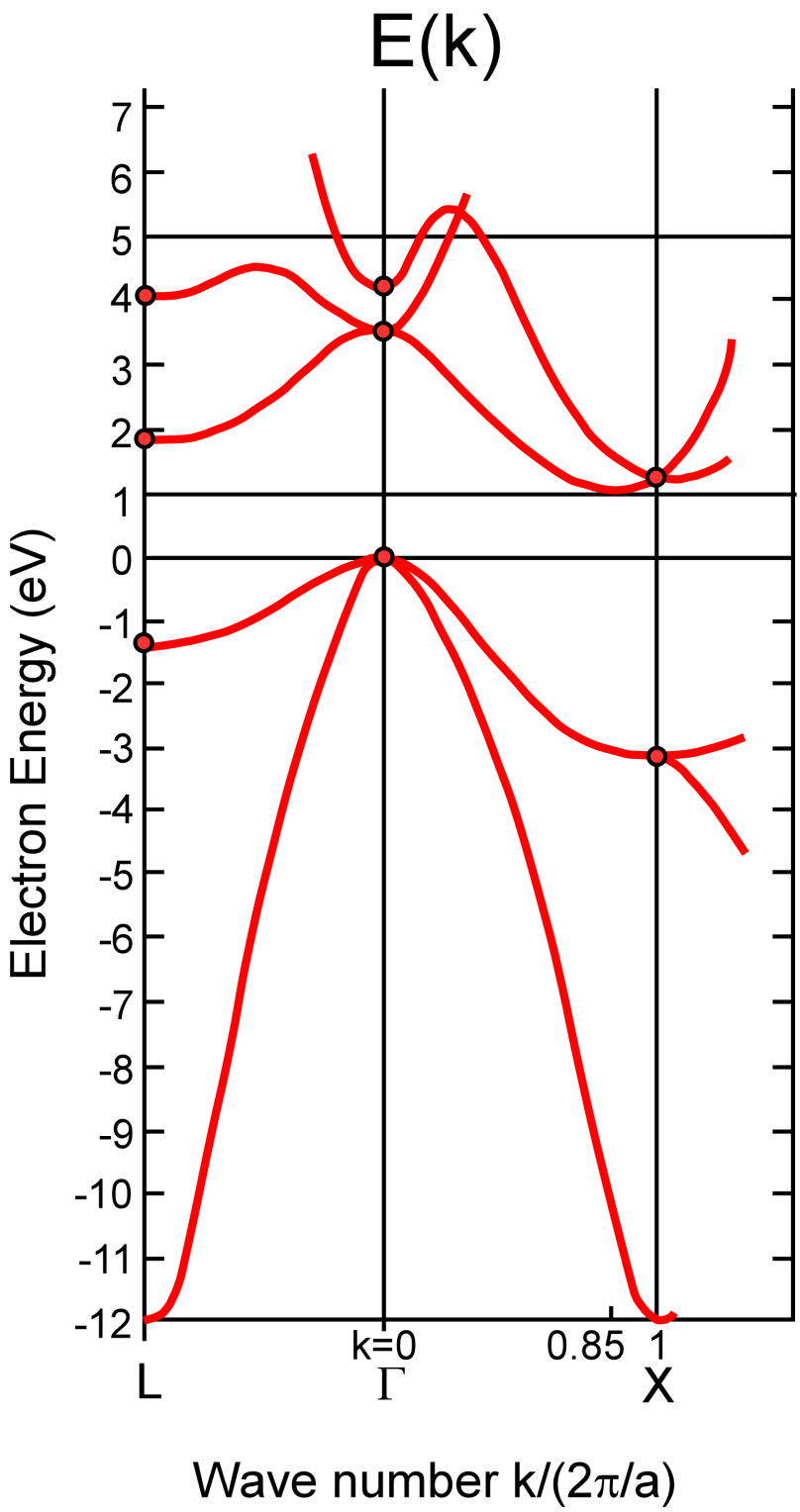

Figure 5.9 The right panel shows E-k diagram of unstrained region-[1] *(6)*.

Figure 5.10 SEM image of single 20 nm wall.

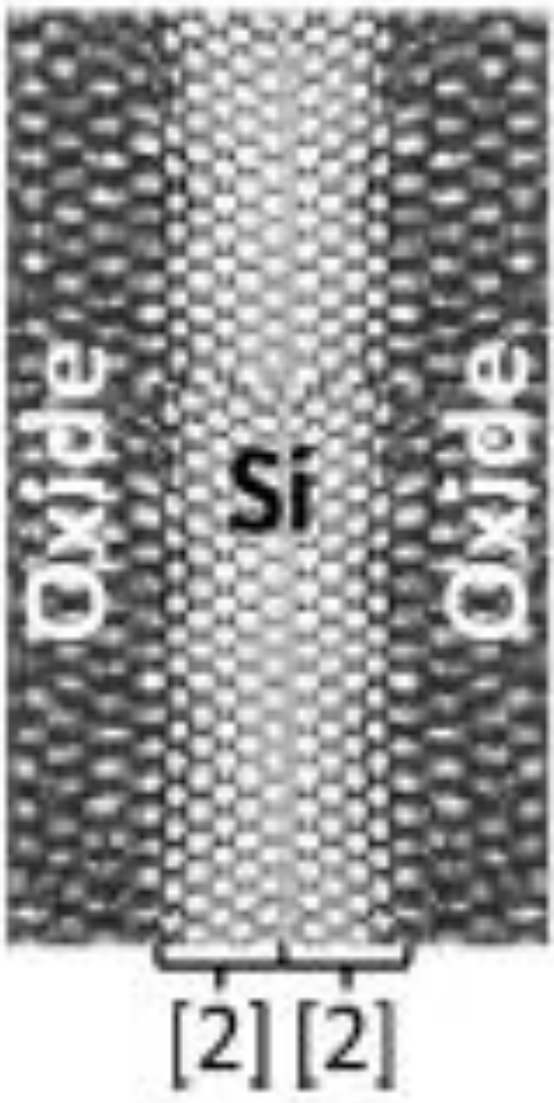

Figure 5.11 Artist's depiction of Si and O atoms shown by light and dark gray spheres, respectively, unstrained region-[1] in the middle has vanished as strained region-[2] closed in from both sides.

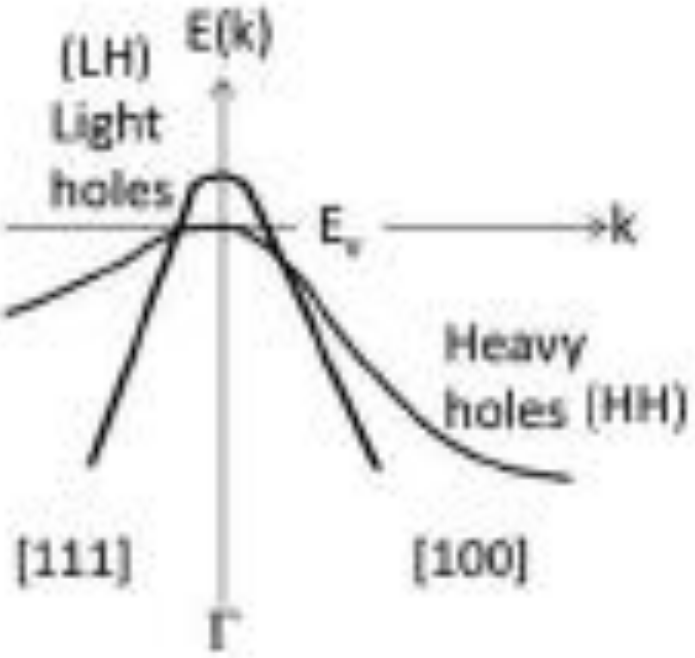

Figure 5.12 The E-k diagram of the strained region-[2].

If we consider a total valence-band hole concentration n_v then, the light-hole (n_{LH}) and the heavy-hole (n_{HH}) concentration will satisfy the charge-conservation relation $n_{LH} + n_{HH} = n_v$, where

$$n_\sigma = \frac{g_\Gamma g_s}{V}\sum_{\boldsymbol{k}}\left[1+exp\left(\frac{E_k^\sigma \mp \eta\Delta E_{str}^v - u_v}{k_BT}\right)\right]^{-1} \approx 2g_\Gamma\left(\frac{m_\sigma^* k_BT}{2\pi\hbar^2}\right)^{3/2} exp\left(\frac{u_v \pm \eta\Delta E_{str}^v}{k_BT}\right), \quad (43)$$

where the subscript σ takes HH or LH and the upper (lower) sign corresponds to HH (LH) state. In the above expressions, the approximations are made for high temperatures, *V* is the volume of the silicon film, *T* is the system temperature, the zero energy is chosen at the middle point between the split pair of light-hole and heavy-hole bands, **k** is the three dimensional wave vector of carriers, $g_\Gamma = 2$ (not *6* due to strain effect) is the Γ-valley degeneracy for holes and $g_s = 2$ is the spin degeneracy for both light-holes and heavy-holes. In addition, u_v, which depends on both *T* and n_V, is the chemical potential to be determined for valence bands, $E_k^{HH} = \hbar^2k^2/2m_{HH}^*$ is the kinetic energy of heavy holes and $E_k^{LH} = \hbar^2k^2/2m_{LH}^*$ is the kinetic energy of light holes, where $m_{HH}^* = 0.49m_0$ and $m_{LH}^* = 0.16m_0$ (m_0 is the free-electron mass) are the effective masses for heavy holes and light holes, respectively. Additionally, ΔE_{str}^v introduced in the above expressions stands for the half of the valence-band splitting due to the existence of strain.

From the above two equations and $n_{LH} + n_{HH} = n_v$, we obtain $n_{LH}/n_v = [1+\gamma^{3/2}\, exp(2\eta\Delta E_{str}^v/k_BT)]^{-1}$ and $n_{HH}/n_v = 1 - n_{LH}/n_v$, where $\gamma \equiv (m_{HH}^*/m_{LH}^*) > 1$. For biaxial and shear strains (7; 8), we have the valence-band splitting, given by

$$\Delta E_{str}^v = \pm\left\{(b^2/2)\left[\left(\epsilon_{xx}-\epsilon_{yy}\right)^2 + \left(\epsilon_{yy}-\epsilon_{zz}\right)^2 + (\epsilon_{zz}-\epsilon_{xx})^2\right] + d^2\left[\epsilon_{xy}^2 + \epsilon_{yz}^2 + \epsilon_{xz}^1\right]\right\}^{1/2} \quad (44)$$

where the upper sign is for the compressive strain while the lower sign for the tensile strain in the direction perpendicular to the interface of silicon and silicon-dioxide materials, *b* and *d* are the optical deformation potentials, and $\epsilon_{jj'}$ represents the strain tensor in the three dimensional space with *j, j'* = *x*, *y*, and *z*, the diagonal matrix elements ϵ_{jj} are associated with biaxial strain, and the off-diagonal matrix elements $\epsilon_{jj'}$ with $j \neq j'$ correspond to contributions from the shear strain. For silicon crystals, we have *b*= *-2.33* eV and *d*= *-4.75* eV.

The values of η can be scaled as $\eta = (1/L)\{\min(L, 2D_s)\}$, where L is the film thickness and D_s is the strain buffering depth due to lattice mismatch between embedded Si crystal and surrounding amorphous SiO_2 material at their interface, and $L - 2D_s > 0$ represents the film effective thickness free of localized trapping centers (9).

If we choose the *z* direction as the direction perpendicular to the interface for biaxial strain we simply get $\epsilon_{xx} = \epsilon_{yy} = \epsilon_{\parallel}$, $\epsilon_{zz} = \epsilon_{\perp}$, and $\epsilon_{ij} = 0$ for $i \neq j$ where $\epsilon_{\parallel} = \left(a_{\parallel,Si}/a_{Si} - 1\right)$, $\epsilon_{\perp} = \left(a_{\perp,Si}/a_{Si} - 1\right)$. Moreover, the perpendicular lattice constant $a_{\perp,Si}$ is related to the parallel lattice constant $a_{\parallel,Si} = \overline{a}_{SiO_2}$ by

$$a_{\perp,Si} = a_{Si}\left[1 - (2c_{12}/c_{11})\left(\overline{a}_{SiO_2}/a_{Si} - 1\right)\right], \qquad (45)$$

where $c_{11} = 16.75 \times 10^{10}\ \mathrm{N/m^2}$, and $c_{12} = 6.5 \times 10^{10}\ \mathrm{N/m^2}$ are the elastic constants of silicon. For silicon and silicon-dioxide, we have $\overline{a}_{SiO_2} = (2 \times 4.914 + 5.405)/3 = 5.078\ \text{Å}$ and $a_{Si} = 5.431\ \text{Å}$ for amorphous silicon-dioxide

materials. Therefore, we obtain $a_{\perp,Si}/a_{Si} = 1.050$. This leads to $\epsilon_{\parallel} = -0.065$ (compressive), $\epsilon_{\perp} = 0.05$ (tensile), and $2\epsilon_{\parallel} + \epsilon_{\perp} = -0.08$.

The total mobility μ_{v} for holes can be expressed as

$$\mu_{\mathrm{v}} = \left(\frac{n_{\mathrm{LH}}}{n_{\mathrm{v}}}\right)\frac{e\tau_{\mathrm{LH}}}{m_0}\left[\frac{m_0}{m^*_{\mathrm{LH}}} + \Delta\left(\frac{m_0}{m^*_{\mathrm{LH}}}\right)\right] + \left(\frac{n_{\mathrm{HH}}}{n_{\mathrm{v}}}\right)\frac{e\tau_{\mathrm{HH}}}{m_0}\left[\frac{m_0}{m^*_{\mathrm{HH}}} + \Delta\left(\frac{m_0}{m^*_{\mathrm{HH}}}\right)\right]$$

$$\approx \left(\frac{n_{\mathrm{LH}}}{n_{\mathrm{v}}}\right)\frac{e\tau_{\mathrm{LH}}}{m^*_{\mathrm{LH}}} + \left(\frac{n_{\mathrm{HH}}}{n_{\mathrm{v}}}\right)\frac{e\tau_{\mathrm{HH}}}{m^*_{\mathrm{HH}}}$$

$$\approx \left(\frac{e\tau_{\mathrm{LH}}}{m^*_{\mathrm{LH}}} + \gamma^{3/2}\frac{e\tau_{\mathrm{HH}}}{m^*_{\mathrm{HH}}}\right)\frac{1}{(1+\gamma^{3/2})} - \gamma^{3/2}\left(\frac{e\tau_{\mathrm{LH}}}{m^*_{\mathrm{LH}}} - \frac{e\tau_{\mathrm{HH}}}{m^*_{\mathrm{HH}}}\right)\left[\frac{\exp(2\eta\Delta E^v_{str}/k_B\,T) - 1}{(1+\gamma^{3/2})^2}\right]$$

$$\approx \mu_v^{(0)}\left[1 - \frac{\eta(2\Delta E^v_{str}/k_BT)\gamma^{\frac{1}{2}}(\gamma-1)}{(1+\gamma^{1/2})(1+\gamma^{3/2})}\right] + \mathcal{O}\left[\left(\frac{\Delta E^v_{str}}{k_BT}\right)^2\right] \qquad (46)$$

i.e., $\left(\mu_v/\mu_v^{(0)} - 1\right) \propto \eta \propto 1/L$, where $\mu_v^{(0)} = (e\bar{\tau}_{\mathrm{v}}/m^*_{\mathrm{LH}})\left(1+\gamma^{1/2}\right)\left(1+\gamma^{3/2}\right)$ is the valence band mobility for $\eta \to 0$, $1/\bar{\tau}_{\mathrm{v}} = (1/2)(1/\tau_{\mathrm{LH}} + 1/\tau_{\mathrm{HH}})$ (with $\tau_{\mathrm{LH}} \approx \tau_{\mathrm{HH}} \approx \bar{\tau}_{\mathrm{v}}$), $|\Delta E^v_{str}| \ll k_BT$ is assumed, the changes in the hole effective masses by strain have been neglected, τ_{LH} and τ_{HH} are the scattering times for light and heavy holes, respectively. It is clear that μ_v increases with $1/L$ for the tensile strain ($\Delta E^v_{str} < 0$) in the direction perpendicular to the interface of silicon and silicon-dioxide materials, as observed by us in Fig. 5.13.

For a given conduction-band electron concentration n_c, the electron chemical potential u_c, which depends on both T and n_c, is decided from

$$n_c = \sum_{\xi=X,L} n_\xi = \frac{g_s}{V} \sum_{\xi=X,L} g_\xi \sum_k \left[1 + exp\left(\frac{E_k^\xi + E_G^\xi - u_c}{k_B T}\right)\right]^{-1}$$

$$\approx 2\sum_{\xi=X,L} g_\xi \left(\frac{m_\xi^* k_B T}{2\pi\hbar^2}\right)^{3/2} exp\left(\frac{u_c - E_G^\xi}{k_B T}\right), \quad (47)$$

where the high-temperature approximation is made in the above expression, $E_{\mathrm{G}}^{\xi} = \varepsilon_{\mathrm{G}}^{\xi}(T) + \eta' \Delta E_{\mathrm{G}}^{\xi}$ is the bandgap energy of strained silicon crystals, which depends on T and the hydrostatic part of the strain, $\varepsilon_{\mathrm{G}}^{\xi}$ stands for the bandgap energy of unstrained silicon crystals, $g_{X,L} = 2$ (not *6* due to strain effect) represents the X (in <100> direction) and L (in <111> direction) valley degeneracy for electroncs at the two minima of conduction band, $E_{\mathrm{G}}^{\xi} = \hbar^2 k^2 / 2m_{\xi}^*$ is the kinetic energy of electrons and m_{ξ}^* is the transverse effective mass of conduction-band electrons with $m_X^* = 0.19\mathrm{m}_0$ and $\mathrm{m}_{\mathrm{L}}^* = 0.1\mathrm{m}_0$. The T dependence of $\varepsilon_{\mathrm{G}}^{\xi}(\mathrm{T})$ (based on the Bose-Einstein phonon model (7)) is given by $\varepsilon_{\mathrm{G}}^{\xi}(T) = \varepsilon_{\mathrm{G}}^{\xi}(0) - 2\alpha_B \Theta_B [coth(\Theta_B/2T) - 1]$, where $\alpha_B = 2.82 \times 10^{-4}$ eV/K is a coupling constant, $k_B\Theta_B$ is a typical phonon energy with $\Theta_B = 351$ K, $\varepsilon_{\mathrm{G}}^{\mathrm{X}}(T) = 1.12$ eV and $\varepsilon_{\mathrm{G}}^{\mathrm{L}}(T) = 2.4$ eV at $T = 300$ K for the *X* and *L* valleys. Moreover, the strain part [2] of the bandgap energy $\Delta E_{\mathrm{G}}^{\xi}$ is calculated as (7) $\Delta E_{\mathrm{G}}^{\xi} = \Xi_d^{(\xi)} Tr(\overleftrightarrow{\epsilon}) + \Xi_u^{(\xi)} \vec{e}_\xi \cdot \overleftrightarrow{\epsilon} \cdot \vec{e}_\xi + aTr(\overleftrightarrow{\epsilon})$, where $\Xi_d^{(\mathrm{X,L})}$ and $\Xi_u^{(\mathrm{X,L})}$ are the deformation potentials of the conduction band for an indirect-gap silicon crystal ($\Xi_d^{(\mathrm{X})} = 1.1$ eV, $\Xi_u^{(\mathrm{X})} = 10.5$ eV for the X valley and $\Xi_d^{(\mathrm{L})} = -7.0$ eV, $\Xi_u^{(\mathrm{L})} = 18.0$ eV for the L valley), $a = 2.1$ eV is the difference of the deformation potentials of conduction and valence bands at two different valleys due to hydrostatic component of the strain for the

silicon crystal, and $\vec{e}_\xi$ is the unit vector pointing to the specific *X* or *L* valley. It is clear from the above equation that $\Delta E_{\mathrm{G}}^{\xi} < 0$ for the tensile strain and $\xi = X$ or L .

The change in the bandgap energy by strain also affects the effective mass of conduction band, given by (10)

$$\Delta\left(\frac{m_0}{m_\xi^*}\right) \approx -\frac{E_P(2\epsilon_\parallel+\epsilon_\perp)\eta'}{\varepsilon_{\mathrm{G}}^{\xi}(T)+\Delta_0/3}\left[2+\frac{3a+3\Xi_d^{(\xi)}+\Xi_u^{(\xi)}}{\varepsilon_{\mathrm{G}}^{\xi}(T)+\Delta_0/3}\right]+\mathcal{O}[(2\epsilon_\parallel+\epsilon_\perp)^2]\,, \qquad (48)$$

where we have neglected the shear strain and assumed a weak strain with $|2\epsilon_\parallel + \epsilon_\perp| \ll 1$, $\Delta_0 = 44$ meV is the spin-orbit splitting and $E_P = 21.6$ eV is the Kane energy parameter.

The total mobility μ_c of conduction-band electrons is obtained as

$$\mu_c = \left(\frac{n_X}{n_c}\right)\frac{e\tau_X}{m_0}\left[\frac{m_0}{m_X^*}+\Delta\left(\frac{m_0}{m_X^*}\right)\right]+\left(\frac{n_L}{n_c}\right)\frac{e\tau_L}{m_0}\left[\frac{m_0}{m_L^*}+\Delta\left(\frac{m_0}{m_L^*}\right)\right] \approx \frac{e\tau_X^0}{m_0}\left[\frac{m_0}{m_X^*}+\Delta\left(\frac{m_0}{m_X^*}\right)\right]^{1+\alpha}$$

$$= \frac{e\tau_X^0}{m_X^*}\left\{1+(1+\alpha)\left(\frac{m_X^*}{m_0}\right)\Delta\left(\frac{m_0}{m_X^*}\right)+\frac{\alpha}{2}(1+\alpha)\left(\frac{m_X^*}{m_0}\right)^2\left[\Delta\left(\frac{m_0}{m_X^*}\right)\right]^2+\cdots\right\}$$

$$= \frac{e\tau_{\mathrm{X}}}{m_X^*}-\eta'(1+\alpha)\left(\frac{e\tau_{\mathrm{X}}}{m_0}\right)\frac{E_P(2\epsilon_\parallel+\epsilon_\perp)}{\varepsilon_{\mathrm{G}}^{\mathrm{X}}(T)+\Delta_0/3}\left[2+\frac{3a+3\Xi_d^{(X)}+\Xi_u^{(X)}}{\varepsilon_G^{\mathrm{X}}(T)+\Delta_0/3}\right]+\mathcal{O}[(2\epsilon_\parallel+\epsilon_\perp)^2]$$

$$= \mu_c^{(0)}\left\{1-\eta'(1+\alpha)\left(\frac{m_{\mathrm{X}}^*}{m_0}\right)\frac{E_P(2\epsilon_\parallel+\epsilon_\perp)}{\varepsilon_{\mathrm{G}}^{\mathrm{X}}(T)+\Delta_0/3}\left[2+\frac{3a+3\Xi_d^{(X)}+\Xi_u^{(X)}}{\varepsilon_G^{\mathrm{X}}(T)+\Delta_0/3}\right]\right\}+\mathcal{O}[(2\epsilon_\parallel+\epsilon_\perp)^2]\,, \quad (49)$$

i.e., $(\mu_c/\mu_c^0 - 1) \propto \eta' + \mathcal{O}(\eta'^2) \propto 1/L + \mathcal{O}(1/L^2)$ (using $\eta' \sim \eta$), where we assume $\tau_\xi = \tau_\xi^0 (m_0 m_\xi^*)^\alpha$ with α labelling the mass dependence in the scattering rate, $\mu_c^{(0)} \approx e\tau_{\mathrm{X}}/m_{\mathrm{X}}^*$ is the conduction-band mobility for $\eta' \to 0$, $\tau_{X,L}$ represents the

scattering times of conduction-band electrons at two different valleys and the high-energy L valley has been assumed depopulated. It is clear that the electron mobility increases with $1/L^2$ in our system with $(2\epsilon_{\parallel} + \epsilon_{\perp}) = -0.08$, as observed by us in Fig. 5.13.

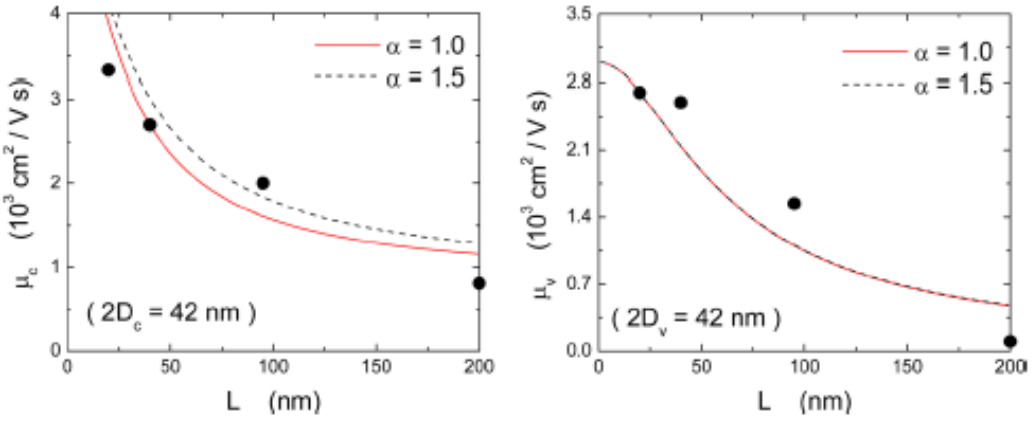

Figure 5.13 Theoretical modeling for electron (left panel) and hole (right panel) mobilities as functions of film thickness L with α = 1.0 (red solid curves) and 1.5 (black dashed curves) and their comparisons with experimental data (black dots) in both panels.

Our numerically calculated results for electron (μ_c) and hole (μ_v) mobilities are presented in Fig. 5.13, along with their comparisons with our experimental data. In our model calculations, we have taken $T = 300\ K$ and the other model parameters can be found from Tables I and II. The good agreement between our numerical calculated results and measured data strongly supports the physical modeling present in this section.

Table 1 Model parameters used in calculating mobility of electrons in strained Si film.

$\mu_c^{max}(cm^2/V\cdot s)$	$\mu_c^{(o)}(cm^2/V\cdot s)$	$\lambda_c nm$	$2D_c(nm)$
5500	806	15	42

Table 2 Model parameters used in calculating mobility of holes in strained Si film.

$\mu_v^{max}(cm^2/V\cdot s)$	$\mu_v^{(o)}(cm^2/V\cdot s)$	$\lambda_v nm$	$2D_v(nm)$
3000	100	143	42

In general, the carrier concentration includes both the doping and photo-excitation contributions. If the sample is undoped, we can simply neglect the impurity scattering and have $n_c = n_v$. The optical-phonon scattering and the inter-valley scattering are only important at high temperatures, while the acoustic-phonon scattering becomes more significant at low temperatures. The surface-roughness scattering, on the other hand, is largely independent of temperature. The detailed calculation of the scattering rate $1/\tau_\xi$ for impurities, phonons, surface roughness and inter-valley can be follows

For the impurity scattering, by using the Fermi's golden rule, its scattering rate $1/\tau_{\text{imp}}$ is calculated as (11; 12)

$$\frac{1}{\tau_{\text{imp}}} = \frac{2}{N_c}\sum_{\boldsymbol{k}} n_k \left[N_i \frac{2\pi}{\hbar}\sum_{\boldsymbol{q}} \left| \frac{-Ze^2}{\epsilon_0\epsilon_r(q^2+Q_s^2)V} \right|^2 \left(1-n_{k+q}\right)\delta\left(E_{k+q}-E_k\right) \right]$$

$$\approx \frac{n_i Z^2 e^4 m^*}{2\pi\hbar^3\epsilon_0^2\epsilon_r^2}\frac{2}{N_c}\sum_{\boldsymbol{k}} n_k \frac{Q_s^2}{k\left(4k^2+Q_s^2\right)^2} \ , \qquad (50)$$

where N_c is the total number of carriers in the system, $n_i = N_i/V$ is the impurity concentration, Z is the impurity charge number, $\epsilon_r = 11.9$ is the Si dielectric constant, $Q_s^2 = (e^2 n_c/\epsilon_0\epsilon_r k_B T)$ at high temperatures with $n_c = N_c/V$, $E_k = \hbar^2 k^2/2m^*$ is the carrier kinetic energy, and m^* stands for the carrier effective mass. For this case, we have $\alpha = 1$. In addition, at high temperatures we get conduction-band electron concentration

$$n_k^e = \frac{1}{1+\exp[(E_k-u_c)/k_B T]} \approx \frac{n_c}{2g_{\text{X}}}\left(\frac{2\pi\hbar^2}{m_{\text{X}}^* k_B T}\right)^{3/2} \exp\left(-\frac{E_k}{k_B T}\right) \ , \qquad (51)$$

where we have assumed the high-energy L valley becomes depopulated. Similar results can be obtained for valence-band hole distributions.

For the longitudinal-acoustic-phonon scattering at high temperatures ($\hbar\omega_q \ll k_B T$), its scattering rate $1/\tau_{ac}$ is calculated (11; 12)

$$\frac{1}{\tau_{ac}} = \frac{2}{N_c}\sum_{\boldsymbol{k}} n_k\{\frac{2\pi}{\hbar}\sum_{q}\frac{\hbar}{2\rho_0 V\omega_q}\left[D_{ac}^2 q^2 + \frac{9}{32}(eh_{14})^2\right]\left(\frac{q^2}{q^2+Q_s^2}\right)^2$$

$$\times\left[\left(1-n_{k+q}\right)N_q\delta\left(E_{k+q}-E_k-\hbar\,\omega_q\right)+\left(1-n_{k-q}\right)\left(N_q+1\right)\delta\left(E_{k-q}-E_k+\hbar\,\omega_q\right)\right]\}$$

$$\approx \frac{2\pi D_{ac}^2 k_B T}{\rho_0\hbar\, v_s^2}\frac{2}{N_c}\sum_{\boldsymbol{k}} n_k g_{3D}(E_k)\ , \qquad (52)$$

where $g_{3D}(E) = m^{*3/2}\sqrt{2E}/\pi^2\hbar^3$ is the three-dimensional density of states of carriers, $N_q \equiv N_0\left(\hbar\,\omega_q/k_B T\right)$, $N_0(x) = 1/[\exp(x)\text{-}1]$ is the Bose function for thermal-equilibrium phonons, $\omega_q = v_s q$, $v_s = 9\times10^5$ cm/s is the sound velocity, $\rho_0 = 2.33$ g/cm^3 is the atomic mass density, $D_{ac} = 5.39$ eV is the deformation potential for acoustic phonons, and h_{14} is the piezoelectric constant neglected. For this case, we have $\alpha = 3/2$.

For the longitudinal-optical-phonon scattering, its scattering rate $1/\tau_{op}$ is calculated as (11) (12)

$$\frac{1}{\tau_{op}} = \frac{2}{N_c}\sum_{\boldsymbol{k}} n_k\{\frac{2\pi}{\hbar}\sum_{\boldsymbol{q}}\frac{\hbar\Omega_0}{2V}\left(\frac{1}{\epsilon_\infty}-\frac{1}{\epsilon_s}\right)\frac{e^2}{\epsilon_0(q^2+Q^2)}$$

$$\times\left[\left(1-n_{k+q}\right)N_{\mathrm{LO}}\delta\left(E_{k+q}-E_k-\hbar\Omega_0\right)+\left(1-n_{k-q}\right)(N_{\mathrm{LO}}+1)\delta\left(E_{k-q}-E_k+\hbar\Omega_0\right)\right]\}$$

$$\approx\left(\frac{D_{op}}{e\ell_{op}}\right)^2\frac{e^2}{8\pi^2\rho_0\Omega_0}\frac{2}{N_c}\sum_{\boldsymbol{k}} n_k[(N_{\mathrm{LO}}+1)g_{3\mathrm{D}}(E_k-\hbar\Omega_0)+N_{\mathrm{LO}}g_{3\mathrm{D}}(E_k+\hbar\Omega_0)]\ , \qquad (53)$$

where $N_{\mathrm{LO}} \equiv N_0\left(\hbar\,\Omega_0/k_B T\right)$, $\hbar\Omega_0 = 63$ meV is the energy of optical phonons, $\left(D_{\mathrm{op}}/e\ell_{\mathrm{op}}\right) = 2.2\times10^{10}$ V/m is the optical-polarization field. For this case, we also have $\alpha = 3/2$.

For the surface-roughness scattering, its scattering rate $1/\tau_{sr}$ is calculated (13)

$$\frac{1}{\tau_{sr}} = \frac{m^*\Lambda^2 e^4 n_{depl}}{\hbar^3 \epsilon_0^2 \epsilon_r^2}\left(\frac{\delta b}{L}\right)^2 \frac{2}{N_c} \sum_{\boldsymbol{k}} n_k \frac{1}{\sqrt{1+k^2\Lambda^2}}\, \mathcal{E}\left(\frac{k\Lambda}{\sqrt{1+k^2\Lambda^2}}\right), \qquad (54)$$

where δb is the average roughness, Λ is the roughness spatial-correlation length in a Gaussian model, and $\varepsilon(x)$ is the complete elliptic integral. Additionally, $(e/\epsilon_0\epsilon_r)n_{depl}$ stands for the surface depletion-charge field, and n_{depl} is the surface depletion-charge areal densities. For this case, we have $\alpha = 1$.

For the inter-valley scattering, its scattering rate $1/\tau_{iv}$ can be calculated in a similar way for phonons, which gives

$$\frac{1}{\tau_{iv}} = \sum_{\xi,\xi'}\left(\frac{D_{\xi\xi'}}{e\ell_{\xi\xi'}}\right)^2 \frac{e^2}{8\pi^2\rho_0\omega_{\xi\xi'}} \frac{2}{N_c}\sum_{\boldsymbol{k}} n_k^{\xi}$$

$$\times\left\{\left[N\left(\omega_{\xi\xi'}\right)+1\right] g_{3\mathrm{D}}^{\xi}\left(E_k^{\xi} - \Delta E_{\xi\xi'} - \hbar\omega_{\xi\xi'}\right) + N\left(\omega_{\xi\xi'}\right) g_{3\mathrm{D}}^{\xi}\left(E_k^{\xi} - \Delta E_{\xi\xi'} - \hbar\omega_{\xi\xi'}\right)\right\}, \qquad (55)$$

where $\left(D_{\xi\xi'}/e\ell_{\xi\xi'}\right)$ is the inter-valley optical-polarization field, $N\left(\omega_{\xi\xi'}\right) \equiv N_0\left(\hbar\,\omega_{\xi\xi'}/k_B T\right)$, $\omega_{\xi\xi'} = v_s\left|\boldsymbol{K}_{\xi'} - \boldsymbol{K}_{\xi}\right|$, and $\Delta E_{\xi\xi'} = E_{\mathrm{G}}^{\xi'} - E_{\mathrm{G}}^{\xi}$. For this case, we have $\alpha = 3/2$.

The finite-size effect in the direction perpendicular to the silicon film becomes significant as $\pi^2\hbar^2/2\mathrm{m}_{\mathrm{X}}^*\mathrm{L}^2 \gg \mathrm{k_B T}$ (14). The existence of such a quantum well modify the splitting of heavy and light holes by $E_{\mathrm{HH}} \rightarrow E_{\mathrm{HH}} + \Delta_{\mathrm{qw}}^{v}$

and $E_{\mathrm{HH}} \rightarrow E_{\mathrm{HH}} - \Delta_{\mathrm{qw}}^{v}$ where $2\Delta_{\mathrm{qw}}^{v}$ stands for the quantum-well induced valence-band splitting, as well as $g_{\Gamma} \rightarrow 1$. It also affects the bandgap energy by $\varepsilon_{\mathrm{G}}^{\mathrm{X}}(T) \rightarrow \varepsilon_{\mathrm{G}}^{\mathrm{X}}(T) + \Delta_{\mathrm{qw}}^{c}$, as well as the density of states of carriers by $g_{\mathrm{3D}}(E_k) \propto \sqrt{E_k} \rightarrow g_{\mathrm{2k}}(E_k) \propto$ constant. Additionally, the coulomb potential in the momentum space is changed by $e^2/\epsilon_0(q^2 + Q^2)V \rightarrow e^2/\epsilon_0(q + q_s)\,A$, where A is the area of the quantum well and $1/q_s$ is the Thomas-Fermi screening length for quantum wells. It is clear that the film quantization effect tends to reduce the strain-induced mobility enhancements of both electrons and holes.

5.4 References

1. **McKelvey, John P.** *Solid State Physics for Engineering and Materials Science.* Malabar, Fl. : Krieger Publishing Company, 1993. ISBN 0-89464-436-X.

2. **Wang, Shyh.** *Fundamentals of Semiconductor Theory and Device Physics.* Englewood Cliffs, NJ 07632 : Prentice Hall, 1989. ISBN: 0-13-344409-0.

3. *Deformation Potentials and Mobilities in Non-Polar Crystals.* **J. Bardeen, W. Shockley.** 1, Murray Hill : Physical Review, 1950, Vol. 80.

4. *Characterization of carrier transport properties in strained crystalline Si wall-like structures in the quasi-quantum regime.* **C. S. Mayberry, Danhong, Huang, G. Balakrishnan, C. Kouhestani, N. Islam, S. r. J. Brueck, and A. K. Sharma.** s.l. : AIP Journal of Applied Physics, 2015, Vols. 118, 134301.

5. *A simple technique for determing the stress at the Si/SiO2 interface.* **Borden, Peter G.** 10, s.l. : Appl. Phys. Lett., 1980, Vol. 36.

6. s.l. : http://large.stanford.edu/courses/2007/ap273/hellstrom1/.

7. **Grundmann, M.** *The Physics of Semiconductors.* s.l. : wnd ed., Springer-Verlag, Berlin Heidelberg, 2010.

8. *Phys. Rev. B 41, 11922.* **Bahder, T. B.** 1990.

9. **E. G. Barbagiovanni, D. J. Lockwood, P. J. simpson, L. V. Goncharova.** s.l. : Appl. Phys. Rev., 2014, Vols. I, 011302.

10. **D. E. Aspnes, M. Cardona.** s.l. : Phys. Rev. B 17, 1978.

11. **D. H. Huang, P. M. Alsing, T. Apostolova, D. A. Cardimona.** .195205, s.l. : Phuys. Rev. B 71, 2005.

12. **G. Gumbs, D. H. Huang.** *Properties of Interacting Low-Dimensional Systems.* s.l. : Wiley-VCH Verlag GmbH & Co., 2011.

13. **T. Ando, A. B. Fowler, F. Stern.** s.l. : Rev. Mod. Phys. 54, 437 , 1982.

14. **Cardimona, D. H. Huang and D. A.** 013822, s.l. : Phys. Rev. A , (2001), Vol. 64.

Chapter 6

CONCLUSION

6.1 Summary and Conclusion

The semiconductor processing, fabrication and the resulting carrier transport characteristics of MSM devices fabricated as wall like structures in silicon on insulator technology were reported. MSM device dark current, DC photocurrents, and the time response of carrier transport were investigated. The resulting conducting channels were actually smaller than their physical dimensions, a result of depletion of carrier near the interfaces, which resulted in a dramatic increase in carrier mobility for both electrons and holes as the physical channel width was reduced from 200 nm to 20 nm. The model showed that by incorporating the effects of strain present in these nanoscale MSM devices the increases in carrier mobilities can be understood. The physical strain altered the energy band diagram of silicon, thereby reducing the carrier effective mass. The contributions of both heavy and light holes were incorporated into the theory and this resulted in an increase of hole mobilities in proportion to $1/L^2$. Likewise, the electron mobilities increase in proportion to 1/L.

6.2 Future work

Natural follow-on work includes the development and characterization of transistors with metallized or polysilicon gates using these wall-like structures. Capture of high mobilities at these nanoscales in a transistor with useful amplification and saturation current could lead to dense circuit topologies if leakage currents, such as sub-threshold leakage and gate tunneling currents are also dramatically reduced. At these nanoscales, the number of dopant atoms in a channel becomes problematic, transistor and switching action may entail an entirely different mechanism than the inversion mechanism that is effective in the metal-oxide semiconductor field effect transistors in use today. The switching action may actually use carrier injection into the channel from source and drain, using the fringing fields from gate to source and drain.

In another area of investigation, the natural extension of two-dimensional confinement can be investigated, leading to a cylindrical transistor with the gate completely enclosing the channel and oxide. The fabrication, experimental and theoretical investigations of these two-dimensionally confined channels, focused on evaluating the enhanced mobility phenomena in the quasi-quantum regime in which the hole mobility tends to coincide with electron mobility, can lead to dramatic enhance in processor speed and dynamic power reduction. In an operating complementary MOSFET inverter, the switching speed is naturally limited by the slowest transistor, and that has historically been the p-channel

device. Investigation of an inverter circuit implemented in a ring-oscillator format will determine whether this is realizable.

Finally, one and two dimensional confinement can be investigated in III-Vs and germanium. The specific conditions (confinement + strain/tensile) for observing this predicted phenomena in these materials requires a very specific device structure geometry, such as a semiconductor nanowire core region (Si or InGaAs or InGaN) that is conformably surrounded by slightly lattice mismatched larger-bandgap cladding material such as (SiO_2 or AlGaAs or AlGaN) respectively. This quasi-1D or 2D systems are different from Van der Waals layered 2D materials since the electron wavefunction can still penetrate into barrier regions, behaving effectively like a bulk material with electronic confinement provided by electrostatic potential barriers. Using these techniques, one can thoroughly investigate the onset of this phenomenon versus feature dimensionality, with nanowire core diameters for this work will ranging from ~200nm down to ~3nm. This range represents the transition region from material bulk properties towards the onset of quantization at room temperature. This investigation will require more complex fabrication techniques but may lead to even more enhanced operation as mobilities are somewhat larger to begin with in some of these materials.